

Caltech Faint Galaxy Redshift Survey XIII: Spectral Energy Distributions for Galaxies in the Region of the Hubble Deep Field North¹

Judith G. Cohen²

ABSTRACT

We introduce a new empirical function for modeling the spectral energy distributions of galaxies. We apply it to a sample of 590 galaxies in the region of the HDF with $z < 1.5$ using multi-color photometry with wide wavelength coverage combined with spectroscopic redshifts from our 93% complete R -selected redshift survey there. We find the following:

- As expected, galaxies with strong signs of recent star formation (i.e. those which show emission lines) have bluer continua in both the rest frame UV and the optical/near-infrared.
- The redder galaxies tend to be more luminous. Although galaxies with strong absorption lines and no emission features are $\sim 15\%$ of the total sample with $0.25 < z < 0.8$, they are $\sim 50\%$ of the 25 most luminous galaxies in the sample at rest-frame R .
- The SEDs of actively star forming galaxies become bluer in the mean in the rest-frame UV at higher redshift, which trend might arise from SED modeling errors. Aside from this, we discern no change with redshift in the relationship between SED characteristics and galaxy spectral type based on the strength of narrow emission and absorption features.
- Combining with similar work at higher and lower redshift, the bluest galaxies have indistinguishable spectral energy distributions in the rest frame ultraviolet over the redshift regime 0 to 3.
- There is no evidence in our R -selected sample that supports the existence of a substantial population of very dusty star forming galaxies at $z \lesssim 1.5$.
- Our ability to predict the mid-IR flux using the UV/optical/near-IR SEDs is limited.
- The potential accuracy of photometric redshifts, bearing in mind that a break at 4000\AA must be detectable to within the errors of the photometry to assign a photo- z for galaxies in this redshift regime, is evaluated.

¹Based in large part on observations obtained at the W.M. Keck Observatory, which is operated jointly by the California Institute of Technology, the University of California and the NASA,

²Palomar Observatory, Mail Stop 105-24, California Institute of Technology, Pasadena, CA 91125

- The rest frame K -band luminosity as a function of redshift clearly shows a gradual change in the population of various types of galaxies, with star forming galaxies becoming both more luminous and a larger fraction of the total population at higher redshift.
- The overall pattern of the $L(K) - z$ relationship suggests that passive evolution at constant stellar mass is a good approximation to the actual behavior of at least the most luminous galaxies in this large sample of galaxies in the region of the HDF out to $z \sim 1.5$.

Subject headings: cosmology: observations — galaxies: fundamental parameters — galaxies: luminosity function — surveys

1. Introduction

In the present paper, we combine the results of our redshift survey in the region of the Hubble Deep Field North (henceforth HDF) (Cohen *et al.* 2000) with multicolor photometric databases to derive the rest frame spectral energy distributions (henceforth SEDs) of the sample’s galaxies. After defining the form of the SED we adopt, and exploring the limits of validity thereof, we concentrate on what can be determined from the behavior of the SED parameters themselves as a function of redshift, galaxy spectral type (i.e. the presence or absence of key emission and absorption features) and luminosity. A comparison of the observed behavior of the SED parameters with the predictions of galaxy evolutionary synthesis models reveals important differences.

The SEDs of the star forming galaxies are then used to constrain possible presence of a substantial population of dusty starburst galaxies and to test our ability to predict the mid-IR thermal emission from dust in star forming galaxies in §5.3. Constraints on the variation in internal reddening from galaxy to galaxy of a given spectral type are derived as well. We compare the rest frame UV SEDs of the bluest star forming galaxies over the regime $z = 0$ to $z \sim 3$.

We also evaluate the ability of photometric redshift schemes to discern the 4000Å break given realistic SED distributions and errors characteristic of ground based photometry in §6. We explore in §7 the conversion from luminosity in the rest-frame infrared into total stellar mass, which relies on a calibration from models of the integrated light of evolving galaxies. A short summary concludes the paper.

As in earlier papers in this series, we adopt the cosmology $H_0 = 60 \text{ km s}^{-1} \text{ Mpc}^{-1}$, $\Omega_M = 0.3$, $\Omega_\Lambda = 0$. Over the redshift interval of most interest, a flat universe with $\Omega_\Lambda = 0.7$ and a Hubble constant of $H_0 = 67 \text{ km s}^{-1} \text{ Mpc}^{-1}$ gives galaxy luminosities very close to those derived below.

2. The Sample of Galaxies

We have recently completed an extensive redshift survey in the region of the HDF. The survey is magnitude-limited, with a selection at R , and objects are observed irrespective of morphology. Redshifts have been obtained for more than 92% of the objects in the HDF (Williams *et al.* 1996) with $R < 24$, and for more than 92% of the objects within a circle whose diameter is 8 arcmin centered on the HDF with $R < 23$. The redshift catalog, presented and described in detail in Cohen *et al.* (2000), contains 671 entries. Hogg *et al.* (2000) (henceforth H00) present a four filter photometric catalog for the region of the HDF including the Flanking Fields, with images in U_n , G and R contributed by C. Steidel, and it is their R catalog that was used to define the samples for the redshift survey.

Appendix A gives an update to this survey with a total of 58 new redshifts, including 5 in the HDF itself. With this addition, the completion of the redshift sample in the HDF itself to $R \leq 24$ is now 95%, while the completion in the Flanking Fields to $R < 23$ is now 93%.

Here we use only the sample of galaxies with $0 < z < 1.5$, eliminating the Galactic stars, the two broad-lined AGN with $z < 1.5$, and the higher redshift ($z \sim 3$) objects³ leaving 590 galaxies. We do this as our ground based photometry is measuring largely the rest frame UV for $z \sim 3$ galaxies and does not provide enough coverage in the infrared to yield an adequate determination of rest frame optical SEDs.

The rest frame UV is very poorly determined in the nearest galaxies with $z < 0.25$ when photometry is limited to ground based photometry without access to space based mid and far UV observations. Hence they are eliminated in the rest of this paper. Although SEDs are determined and tabulated for galaxies with $z < 0.25$ here, we will utilize in the subsequent discussion the sample of galaxies restricted to the range $0.25 < z < 1.5$, which contains 552 galaxies of which 107 are in the HDF itself.

The results presented throughout this paper are robust to the elimination of the fainter galaxies in the HDF, where the sample is deepest.

2.1. The Redshift Ranges

The present sample of galaxies in the region of the HDF with $0.25 < z < 1.5$ and with SEDs considered reliable contains 519 galaxies, of which 105 are in the HDF itself.⁴ These are divided into four redshift ranges: “low” ($0.25 \leq z < 0.5$), “mid” ($0.5 \leq z < 0.8$), “high” ($0.8 \leq z < 1.05$), and “highest” ($1.05 \leq z \leq 1.5$). In the “highest” redshift range, the assignment of galaxy spectral

³The two AGNs with $z < 1.5$ are sometimes included in the figures.

⁴In §3.8 we find that 33 of the galaxies have SEDs not considered reliable.

classes is less accurate (see the discussion in Cohen *et al.* 1999a) and the redshift completeness is affected by the fact that the intrinsically strong [OII] 3727Å emission line is shifted into the region beyond 7500Å, where strong night sky emission lines make detection of faint emission lines from distant galaxies more difficult.

3. The Derivation of the SEDs

The derivation of the spectral energy distribution for a galaxy requires a set of photometric measurements for the object with N filters, a set of effective wavelengths and flux zero point calibrations for the filters, and a model for fitting the SED. Our goal is an overall characterization of the SED suitable for the determination of luminosity functions given the fact that we are dealing to a large extent with ground based photometry of faint galaxies.

We are trying to obtain a set of redshift independent parameters characterizing the rest frame SED of a galaxy from a set of observations made at filter bandpasses fixed in the observed frame. We would like to be able to use our SED model parameters to predict fluxes of galaxies from 2400 Å to 2.2μ in the rest frame over the redshift range $0.25 \leq z \leq 1.5$ with an accuracy of 25% (0.1 dex).

The complexity of the SED model to be used here is restricted by the limited photometry available for these objects, both in terms of accuracy for these faint galaxies and also in wavelength sampling. Were we dealing with HST data only (for the same set of filters) or with much brighter galaxies, a much more sophisticated approach such as that of Budavári *et al.* (2000) would be justified.

3.1. The Sources of Photometry

Since the catalog of H00 was used to define the sample for the redshift survey of Cohen *et al.* (2000) and since it provides four filter photometry (U_n , G , R and K_s) for the entire sample, we adopt it as the primary photometric source. The H00 photometry is consistent to within the uncertainties with the more accurate photometry of Williams *et al.* (1996) for objects in the HDF itself for the optical colors. In the Flanking Fields around the HDF, we supplement the photometric database of H00 with the I and K measurements of Barger *et al.* (1998). We utilized primarily I from Barger *et al.* (1998) to fill in gaps in the wavelength coverage of H00. For the faintest objects (in the infrared) in the Flanking Fields, we used K as well, as the limiting magnitude of the Barger *et al.* (1998) database is fainter at K than that of H00. The U , B , V , R bands of Barger *et al.* are used to supply added confidence in the U_n , G , R photometry of H00. Thus, for an object in the Flanking Fields, there is a maximum of 10 observations, with two independent measurements for three colors (U , R and K), hence seven distinct filter bandpasses.

Within the HDF, in addition to the photometric catalog of H00, we also use the I, J, H, K photometry of Fernandez-Soto, Lanzetta & Yahil (1999). Their catalog is based on the HST images of the HDF with the F814W filter for I , and on their analysis of IR images of the HDF from KPNO described in Dickinson (2000). The red end of the SED is thus better determined for galaxies in the HDF itself, due to the existence of the J and H photometry and the very high quality of the F814 HST images compared to ground based I images.

The H00 and Fernandez-Soto, Lanzetta & Yahil (1999) photometric databases appear to be consistent with each other. They both use the SExtractor code (Bertin & Arnouts 1996) for object selection, and both have a scheme to handle extended objects, yet still preserve accuracy for the smallest and faintest galaxies. The unpublished photometry of Barger *et al.* (1998) treats the extrapolation to the total magnitude of extended objects differently from the procedure adopted in H00.

We have adopted a single effective wavelength for each filter for all objects irrespective of their spectral indices, ignoring any dependence of λ_{eff} on the color of the object. This is a reasonable assumption given the precision of our photometry for faint objects and the desired precision of the SED indices to be derived. The effective wavelengths of the various filters are given in an appendix.

Once the effective wavelengths were defined, the zero points of the observed flux f_ν for the Vega-relative photometry were taken from Fukugita, Shimasaku & Ichikawa (1995). The HDF photometry of Fernandez-Soto, Lanzetta & Yahil (1999) is already presented in the form of observed flux per unit frequency f_ν .

A small extinction of $E(B-V) = 0.012$ mag was adopted based on the maps of Schlegel, Finkbeiner & Davis (1998); appropriate corrections were applied to each filter.

Our photometric database covers U through K in the observed frame. The red end of this corresponds to 0.9μ in the rest frame of the highest redshift considered here and to $\sim 1.3\mu$ for a more typical $z \sim 0.7$ galaxy. Prediction of fluxes in the rest frame redward of 0.9μ requires trusting the parametric form of our adopted SED model described below for the highest redshift galaxies in the sample.

3.2. The Dual Power Law Model for the SEDs

We initially adopted the same form for SEDs as in Cohen *et al.* (1999a), namely we assume that the emitted luminosity per unit frequency in the rest frame over the wavelength regime 0.2 to 1.6μ can be represented by a power law whose index may change at 4000\AA . Thus L_ν , with units of Watts/Hz, is assumed $\sim \nu^{-\alpha}$ with an index in the region redward of 4000\AA (in the rest frame) denoted α_{IR} and an index in the rest frame UV of α_{UV} . Three parameters are required to characterize each SED. We refer to this as the 2p SED model.

Several tests of the validity of this model have been made to establish the wavelength range over which it can represent galaxy SEDs with the requisite degree of precision. Both SEDs from calculations of the integrated light of evolving galaxies and SEDs interpolated from spectrophotometric and broad-band photometric observations of nearby galaxies have been used in these trials. In the first test, we fit the galaxy evolution models of Poggianti (1997), using the filter transmission curves for the set of filters for which photometric catalogs exist in the region of the HDF. Figure 1a illustrates SEDs from Poggianti of a local elliptical, Sa and Sc galaxy (henceforth denoted as the standard set of test SEDs) observed at $z = 0.6$. The observed filter bands are the large circles plotted at their appropriate rest wavelengths. While the spectral region beyond the 4000Å break for all the models from Poggianti that were examined is well represented by a single power law with deviations never exceeding 0.1 dex, the 2p model systematically predicts too much flux beyond 1.7μ .

Tests of the 2p model were also carried out with galaxy SEDs predicted from Worthey (1984) and with a set of SEDs of nearby galaxies of various morphological types constructed by G. Neugebauer (private communication, 2000) based on observations in the the UV and optical assembled by Coleman, Wu & Weedman (1980) supplemented with broad-band IR photometry from Aaronson (1978) and from Frogel *et al.* (1978). In all cases the 2p SED overpredicts the flux in the near infrared.

We compare the predicted flux at an observed wavelength of 3.2μ from our SED model with those galaxies in the HDF with detections at that wavelength from Hogg *et al.* (2000). Given the typical redshift of these galaxies of $z \sim 0.5$, these observations have a typical rest wavelength of 2.1μ . Again, the 2p model for the SED overpredicts the observed flux for the 9 galaxies with detections by about a factor of two.

This deviation in the near infrared between the power law and the galaxy flux presumably largely arises because one is then well into the long wavelength tail of a black-body distribution, where even for T as low as 4000K, f_λ is no longer rising rapidly with λ .

In the UV, the high spectral resolution of the Poggianti model grid demonstrates the existence of a different possible concern. Many of Poggianti's models show f_λ falling shortward of of the 4000Å break, and then rising again as flux from the youngest and hottest stars begins to contribute substantially. This curvature obviously cannot be reproduced well by a single power law flux in the UV.

These tests demonstrate that the 2p model SED is at best marginally adequate for our purposes.

3.3. A New Empirical Model for Galaxy SEDs

To avoid the difficulties of 2p SED model described above, we have developed a new model for galaxy SEDs. One natural way to introduce the desired curvature in the optical and near IR spectra region is to replace the power law with a black body function. However, the peak of the Planck function itself is too narrow to give a good fit to actual galaxy SEDs, as one might expect for a composite stellar population containing stars with a range of effective temperatures. The empirically determined function we adopt as our SED model, which provides a simple but versatile parameterization of galaxy SEDs with parameters that are physically motivated, has a mathematical form which we denote as a “stretched black body” (henceforth sBB). We apply the sBB function to fit the optical/near IR, while we retain a power law fit to the UV.

A wavelength λ_m is specified as the wavelength at which the fit function changes. The “stretched wavelength” λ_s corresponding to a rest frame wavelength λ_0 is then defined as

$$\lambda_s = \lambda_m + (\lambda_0 - \lambda_m)/f,$$

for $\lambda_0 \geq \lambda_m$, where f is the stretch factor. To evaluate the sBB Planck function, the “stretched wavelength” is converted to a frequency in the usual way, $\nu_s = c/\lambda_s$, and then used in the calculation. This applies to both the ν^3 and exponential part of the Planck function, as well as the ν multiplier required to obtain luminosities. The temperature used in the Planck function is denoted as $T(sBB)$. The details of the fitting procedure are given in an appendix.

It is important to note that in this model, unlike in the 2p SED model, the flux at λ_m from the red fit and from the blue fit is not automatically constrained to be the same. This offers the possibility of direct measurement of the the 4000Å break which in cool stars is due to enhanced absorption by metal lines and in hotter stars by the Balmer jump. An sBB fit thus has four parameters, α_{UV} , $T(sBB)$, the blue side luminosity and the red side luminosity, both at λ_m . As described in the appendix, depending on the number and distribution with wavelength of the available filter bandpasses (i.e. photometric catalogs), the two luminosity parameters are not always independent.

There are two constants in a sBB fit, λ_m and the wavelength stretching factor f . Their values were determined by optimizing χ^2 when a sBB fit was applied to the standard test set of Poggianti’s (1997) local galaxy SEDs observed at $z = 0$ and at $z = 0.6$. The resulting choices adopted henceforth for sBB fits are $\lambda_m = 4050 \text{ \AA}$ and $f = 1.6$.

Figure 1b shows the sBB fit to the set of standard test SEDS, i.e. the same SEDs as is shown in Figure 1a. The sBB fit solves the problem of overpredicting the rest frame flux at K and, with only one extra parameter, the sBB model shows a much better fit overall to predicted galaxy SEDs, as well as allowing a measurement of the 4000 Å break.

3.4. The Stability of the SED Parameters with Redshift

The model SED must measure the same values for its parameters irrespective of the redshift of a galaxy. Otherwise the flux cannot be predicted reliably at a fixed rest wavelength. This is particularly difficult at K , as we are then extrapolating beyond the rest frame wavelength range of the available photometry for $z > 0$. As pointed out by the referee, the 2p SED model fails this test. Figure 2 shows the output parameters from this model, α_{UV} and α_{IR} , applied to the set of standard local test SEDs as the redshift of observation is varied from 0 to 1.5. (The dependence of α_{UV} in the region $z < 0.25$ should be ignored; see §2.) Note the large changes in output parameters for the 2p model SED as the redshift at which the galaxy is observed is varied.

This translates into predictions of flux using the 2p SED model which are, at the extremes of the rest wavelength range covered, so different from the those of the actual SED that our accuracy tolerance is grossly exceeded. Figure 3 shows the deviation from the fluxes of the standard test set of local SEDs predicted by the 2p SED model as the observations are carried out over the redshift range of interest, from $z = 0$ to $z = 1.5$. Results at four rest wavelengths, the two wavelength extremes of our range, 2400 \AA and 2.2μ , as well as at two intermediate wavelengths, 4350 and 7900 \AA , are illustrated. As expected, the ability of the 2p SED model to predict the flux at the extreme ends of the wavelength range is poor, although in the central part of the wavelength range it is reasonably good.

Figures 4 and 5 show the equivalent tests applied to the sBB model. Note that Figures 3 and 5 are directly comparable; the same rest wavelengths, axis scales and plot symbols are used in both cases. We see that the predictive ability of the sBB fit is quite good; over the full redshift range $0 < z < 1.5$, the rest frame flux at K is predicted to within ± 0.1 dex (our required tolerance), while the rest frame flux at 2400 \AA is predicted almost as accurately for $0.25 < z < 1.5$.

At this point, with the sBB fits, the worst remaining problem is now in the rest frame UV (see figure 4). The overall trend towards measuring a bluer $\alpha(UV)$ as z increases, particularly for the Sa and Sc SEDs, is probably due to an attempt to fit a curved SED which is “convex upward” as the contribution from younger stars increases and changes the curvature. In spite of this, we note that the flux prediction of the sBB model at 2400 \AA shown in Figure 5 is still close to or within our tolerances.

These tests have been repeated for the sBB model omitting the J and H band coverage, as occurs in the Flanking Fields of the HDF in contrast with the HDF itself, where J and H photometry is available. The sBB fits are still very good and remain within the specified tolerance until $z > 1.1$.

3.5. Final Comments on the SED Models

Extrapolation beyond rest-frame K or blueward of 2400 Å of our adopted form for galaxy SEDs is not appropriate.

Additional data on the 1.5 to 5 μ SEDs of nearby galaxies at better spectral resolution than is provided by standard broad band infrared photometry would be helpful for improving the accuracy of galaxy synthesis models in the near IR.

3.6. Reddening

We have tried adding additional reddening to the SEDs of local galaxies, both synthesized from models and observed. As one might expect, an additional reddening of $A_V = 1$ mag with the standard Galactic extinction curve produces an increase in α_{UV} of ~ 2 and an increase in α_{IR} of ~ 0.5 . The fit over the wavelength range of interest is degraded, although not beyond the limit of acceptability until the additional A_V reaches 2 mag. As we will see later, the range of the indices α_{UV} and α_{IR} within each galaxy spectral type is sufficiently small that a range in reddening within each galaxy spectral type significantly exceeding $\sigma(A_V) = 1$ mag can be ruled out. However, a much larger range in reddening can be tolerated if it is grayer than the standard Galactic extinction curve, and has, for example, the form advocated by Calzetti (1997).

3.7. Construction of the SEDs

The SEDs for the galaxies in the region of the HDF were constructed by calculating for each filter bandpass for which photometry exists the quantity $\nu L_\nu = 4\pi D_L^2 \nu f_\nu = \nu_0 L_{\nu_0}$, where ν is the observed frequency and ν_0 is the rest frame frequency. (D_L is the luminosity distance in our adopted cosmology.) We then shift the observed effective wavelengths into the rest frame. For each galaxy a plot was made of the raw SED which was then inspected manually. For about 10% of the objects, one deviant point, presumably corresponding to one bad measurement, was adjusted. In addition, the difference in large aperture extrapolation between the H00 and Barger *et al.* datasets had to be removed. Our magnitude zero point is based on that of H00.

A fit to the set of N values νL_ν for each galaxy was then attempted. Details of fitting procedures and how the luminosity at the matching point is handled are given in an appendix.

The resulting parameters for each galaxy for the 2p SEDs are the rest frame emitted luminosity at B , $L(B) \equiv \nu L_\nu$ evaluated at B in the rest frame and the two power law indices. The range of $\pm 1\sigma$ values for α_{UV} was from 0.2 to 0.9, with a typical value ~ 0.5 in the Flanking Fields and ~ 0.4 in the HDF itself. For the sBB fits, the resulting parameters are α_{UV} , T , and $L(\lambda_m : \text{blue})$ and $L(\lambda_m : \text{red})$. These values are given in Table 1 for our sample.

3.8. Special Cases

A number of special cases arose for very faint or very crowded objects in the Flanking Fields. If there was no detection of a galaxy at 2.2μ , then the median value of the IR parameter for that redshift range and galaxy spectral type (see §4) was adopted for the object. A check was made to be sure that this value was consistent with the limit of $K \sim 20$ of the H00 photometric survey and of the somewhat fainter limit for the Barger *et al.* (1998) survey.

If the object was very crowded, usually the fainter of a close pair on the sky, the H00 database only contains a R mag, which was estimated after the main database was assembled during the cross checking of the redshift catalog with the photometric catalog (see Cohen *et al.* 2000 for details). In such cases, the relevant median was adopted for each of the SED parameters. The rest frame B luminosity was then the only parameter calculated from the limited observations available.

There are a total of 33 such objects. These galaxies are not included in Table 1 nor in any plots of the spectral indices or calculations of their properties, but will be included in calculating the luminosity function in a future paper.

With two exceptions, we were able to determine reliable SEDs for all the galaxies with redshifts within the HDF itself.

4. Properties of the SEDs

We discuss the properties of the SEDs as a function of redshift, luminosity, galaxy star formation rate, etc. To demonstrate that the results are robust, we retain both the 2p and the sBB fits in the tables, but since the sBB model for galaxy SEDs is clearly superior, only those fits are shown in the remaining figures. We use the galaxy spectral classification scheme defined in Cohen *et al.* (1999b), which basically characterizes the strength of the strongest emission lines, particularly [OII] at 3727 \AA , [OIII] at 5007 \AA and $H\alpha$ relative to the strong absorption features, H and K of CaII and the normal absorption in the Balmer lines. To review briefly, “ \mathcal{E} ” galaxies have spectra dominated by emission lines, “ \mathcal{A} ” galaxies have spectra dominated by absorption lines, while “ \mathcal{T} ” galaxies are of intermediate type. Galaxies with broad emission lines are denoted as spectral class “ \mathcal{Q} ”. Starburst galaxies showing the higher Balmer lines ($H\gamma$, $H\delta$, etc.) in emission are denoted by “ \mathcal{B} ”, but for such faint objects, it was not always possible to distinguish them from “ \mathcal{E} ” galaxies. These classifications were assigned for the galaxies our sample in the region of the HDF in Paper X (Cohen *et al.* 2000).

To illustrate our SEDs applied to real galaxies, Figure 6 shows the SEDs for the five sources in the HDF detected by Chandra (Hornschemeier *et al.* 2000) included in our sample. The mid-IR luminosities determined from ISO observations by Aussel *et al.* (1999) and the VLA radio luminosities inferred from the work of Richards *et al.* (1998) and Richards (2000) are shown as

well when the galaxies were detected. The X-ray detections are in galaxies with spectral classes \mathcal{Q} (a broad lined AGN), \mathcal{A} , \mathcal{I} , \mathcal{EI} and \mathcal{E} , i.e. three of the five do not show have strong narrow emission lines, hence do not show evidence for a high current rate of star formation.

4.1. The Correlation between SED Parameters and Galaxy Spectral Types

Table 2 gives the medians of α_{UV} and α_{IR} from the 2p model SED over the four redshift ranges and for various spectral classes of galaxies. Table 3 provides the same for the parameters α_{UV} and T from the sBB model. ($\log(T)$ is actually used.) Only galaxies with reliable redshifts (redshift quality class 1, 2, 4 or 6, see Cohen *et al.* 1999b for definitions) are used, as is true for all subsequent tables and figures.⁵ While the distribution of these indices is non-Gaussian, we have used the first and last quartiles of the distribution in each case to produce a corresponding σ assuming a Gaussian distribution prevails.

The dispersion for each galaxy spectral type is a combination of the intrinsic dispersion and that induced by variations in internal reddening from galaxy to galaxy as well as the known uncertainties in determining the SED parameters. Making the absurd assumption that the first and last factors are negligible, these values of σ can be used to set firm upper limits on internal reddening variations within galaxies. If one assumes a Galactic extinction law, then $\sigma(A_V) \sim 1$ mag will reproduce the observed range in α_{IR} for each of the three galaxy spectral classes. Again assuming a Galactic extinction law, the dispersion in reddening required to reproduce the range of α_{UV} is about 1/3 as large. The adoption of a grayer reddening curve will allow a larger range in A_V .

As expected, the galaxy spectral classes are correlated with the overall SED shape. “Bluer” galaxies (those with bluer continua) tend to show have stronger emission lines, while redder galaxies tend not to have detectable emission lines. This is apparent in the local Universe, and we reaffirm this again at much higher redshift. This is true not only for the rest-frame UV continuum, but also for the rest-frame Paschen continuum, although the effect is smaller there. The observation that galaxies with strong emission lines (i.e. those with strong current star formation) are bluer is one found by many other surveys, both locally and within the redshift range under discussion here, e.g. Lin *et al.* (1996) for the Las Campanas Redshift Survey, Ellis *et al.* (1996) for the LDSS survey, Cowie *et al.* (1996), Hammer *et al.* (1997) for the CFRS.

Figure 7 shows a plot of the two sBB SED parameters α_{UV} and T for galaxies in the “mid” and the “high” redshift ranges. This figure (when constructed using the 2p SED model parameters) looks very similar to the corresponding figure (Figure 5) of our analysis of data from our survey field at J0053+1234 given in Cohen *et al.* (1999a). As would be expected from Tables 2

⁵Unless otherwise specified, starbursts (galaxy spectral type \mathcal{B}) are included with the \mathcal{E} galaxies. Broad-lined AGNs are excluded throughout.

and 3, galaxies whose spectra are dominated by emission lines occupy a different area in this plot than do the galaxies without detectable emission lines. Again as expected, galaxies with strong emission lines are significantly bluer in the rest-frame UV and somewhat bluer in the rest frame optical/near IR, while galaxies with no sign of ongoing star formation are redder in both in the rest frame UV and in the Paschen continuum.

To reinforce this point, a histogram of SED indices with galaxy spectral type for galaxies in the “mid” and “high” redshift range is shown in Figure 8a, 8b.

4.2. The Correlation between SED Parameters and Redshift

Table 2 and Table 3 demonstrate a decrease of α_{UV} with increasing redshift for \mathcal{E} galaxies which is in the expected sense, i.e. higher redshift star forming galaxies appear bluer in the rest frame UV than their local counterparts, probably due to a higher contribution to the total galaxy luminosity from young stars, i.e. a higher mean star formation rates per unit galaxy luminosity. One may also attribute this change to the limited ability of even the sBB model to produce for a fixed galaxy SED a constant value of $\alpha(UV)$ as a function of redshift (see figure 4).

However, with the exception noted above, the UV and optical/near IR SED indices (α_{UV} and α_{IR} or T) appear to be constant with redshift for each of the three major galaxy spectral classes, \mathcal{A} , \mathcal{I} , and \mathcal{E} , to within the uncertainties defined by assuming that the scatter has a Gaussian distribution for the “low”, “mid” and “high” spectral ranges. The CFRS group (Hammer *et al.* 1997) also found only modest evolution in mean colors with redshift.

The rest frame optical/near IR continua of \mathcal{E} galaxies appear to become somewhat redder at high redshift, but this is dependent on the median of T or α_{IR} for the highest redshift bin. It is not surprising that the \mathcal{E} galaxies in the the “highest” redshift range appear to have somewhat redder rest-frame optical continua, as at that point the galaxy spectral classification becomes unreliable, and the \mathcal{E} class is a catch-all for a wide range of galaxies. Similar concerns manifest themselves for the highest z -range in which I galaxies could be detected.

This result is equivalent to stating that the association between the spectral indices that characterize the continuum slopes of the median rest frame SED of galaxies and the presence of certain discrete narrow spectral features (i.e. those that define the galaxy spectral classes \mathcal{A} , \mathcal{I} , and \mathcal{E}) is roughly invariant out to $z \sim 1.1$, with the exception that actively star forming galaxies become bluer in the UV at higher redshift.

We can compare the behavior of the SED parameters with redshift with that predicted by Poggianti’s (1997) galaxy evolutionary synthesis models. We apply the same procedure to determine the power law indices to these galaxy models, assuming that her E, Sa, and Sc models correspond roughly to our galaxy spectral classes \mathcal{A} , \mathcal{I} , \mathcal{E} . Her elliptical models show SEDs that change little with age, at least to $z \sim 1$, in accordance with the data shown in Table 2. This

corresponds to the well known difficulty of determining the age of an old stellar population from broad band photometry alone.

However, Poggianti’s Sa and Sc models become bluer at all wavelengths within the range of interest more rapidly between $z \sim 0$ and $z \sim 1$ than do the galaxy SEDs in our sample. This difference is significantly larger than the uncertainties.

Galaxy evolutionary synthesis calculations involve many theoretical inputs and many assumptions, with only a limited number of constraints applying, mostly at $z = 0$. One expects that the errors in stellar evolutionary tracks or in our cosmology (i.e. in the relationship between redshift and age) will not be substantial. However, errors in the synthesis models arising from the forms adopted for the star formation rate as a function of time (i.e. at $z > 0.5$) for the various current galaxy spectral classes may be more serious.

An interesting possibility for a partial explanation is a scenario where as galaxies evolve in time, their SEDs age, and their morphological classifications may also evolve. Van den Bergh, Cohen, Hogg & Blandford (2000), among others, present evidence from an analysis of the morphology of this sample of galaxies on the HDF images taken by HST supporting morphological evolution of galaxies with redshift.

The most likely explanation of this difference between the behavior with redshift of the SED parameters of our sample, divided in spectral classes, and predictions of galaxy evolution models is the star formation rate of a particular model galaxy from Poggianti (1997) varies so much with time out to $z \sim 1.5$ that as their SEDs age the galaxies will shift between the relatively small number of galaxy spectral classes used here. This is an issue that will be explored in future work.

4.3. The Correlation of Luminosity with Color

In Cohen *et al.* (1999a) we found a tentative relationship between spectral slopes and galaxy luminosity such that more luminous galaxies are redder, suggestive of a continued correspondence at high z to the well known galaxy luminosity - mean metallicity relationship shown by early type galaxies in the Local Universe. (See, for example, the discussion of spiral galaxies in Zaritsky, Kennicutt & Huchra 1994, and for the dwarf galaxies in the Local Group see Côté, Oke & Cohen 1999). The large range in star formation rates among galaxies will also contribute to a relationship between SFR and luminosity if most star formation is now occurring within low luminosity galaxies. Such galaxies would then appear bluer than high luminosity more quiescent galaxies (see, e.g. Boselli *et al.* 2000).

We now examine our much larger data set in the HDF to see if this trend persists. We construct the rest frame optical luminosity using the parameters from the SED fit for each galaxy. For the 2p SED model, we use rest frame R , while for the sBB model, we use $L(\lambda_m : \text{red})$. Even for the highest redshift galaxies in this sample, rest frame R lies within the range of the existing

broad band photometry, so no extrapolation of the SED is required.

The results are given in Table 4 for the 2p SED model and Table 5 for the sBB SED model. The luminosity characteristic of each redshift range rises with increasing z for the redshift range, as is expected since ours is a magnitude limited sample. There is a clear trend of galaxies with redder UV power law indices (larger α_{UV}) being more luminous in every redshift range except in the highest range, see Figure 9. The increase in median rest frame optical luminosity from the bluest to the reddest galaxies in each redshift range is about a factor of 5.

The same trend is present for the IR power law indices, but the increase is by a smaller factor, about 3, from the bluest to the reddest galaxies.

The highest redshift range behaves anomalously, but that is not surprising, as only the most luminous galaxies can be detected there at such high redshifts, and the depth in luminosity of the sample is small. Furthermore, it is very difficult to assign redshifts beyond $z \sim 1$ to systems dominated by strong absorption lines, which are the most luminous galaxies in the lower redshift ranges; any such galaxies may be so red as to fall below the R cutoff of our sample.

To summarize, the reddest galaxies in both the rest frame UV and optical/near-IR tend to be the most luminous, at least to $z = 1.05$, after which, such a trend, if present, would be very hard to establish from our sample. For example, of the 25 most luminous (in rest frame R) galaxies with $0.25 < z < 0.8$, 12 have been assigned to galaxy spectral class \mathcal{A} , but less than 15% of the total sample within that redshift range is assigned to this spectral class.

This is a well established trend in the local Universe, shown clearly in the recent large samples from the SDSS and 2dF surveys analyzed by Blanton *et al.* (2000) and by Folkes *et al.* (1999) respectively.

Since this is true in the rest frame optical, the effect will be even larger at rest frame K , which is a better measure of the true luminosity of the stellar system, unperturbed by contributions from a small number of bright young (blue) stars.

We thus see a picture of quiescent non-star forming galaxies being the most luminous at each z , while star-forming galaxies are bluer and also in each of the redshift ranges up to $z \sim 1.1$ have on average significantly lower rest frame optical (and even more so K) luminosities.

5. Properties of the SEDS of the \mathcal{E} Galaxies

Our selection of star forming galaxies is complete, in that all objects with strong emission lines are included in the \mathcal{E} spectral class. We would see strong emission lines if such were present

in any galaxy of *any* spectral slope with $z < 1.2$ ⁶ if that galaxy fell within our magnitude-limited survey.

5.1. The UV SEDs of Starburst Galaxies from $z \sim 0$ to $z \sim 3$

Calzetti, Kinney & Storchi-Bergmann (1994), in their study of local starburst galaxies, define the UV extinction in terms of the spectral power law index β derived for f_λ , where in terms of our UV index α_{UV} , $\beta = \alpha_{UV} - 2.0$. Their latest calibration of β versus $E(B - V)$ and versus absorption at 1600\AA is given in Meurer, Heckman & Calzetti (1999). Their data demonstrate that local starbursts have $-0.5 < \alpha_{UV} < +2.5$, with a median of ~ 0.6 .

There are too few spectroscopically identified starbursts in our sample to examine their SED properties.⁷ Instead we consider the SED properties of the entire population of \mathcal{E} galaxies. Figure 8a shows that for the “mid” and “high” redshift group (as is true also of the other two redshift groups) there is a falloff on the blue side of the distribution of α_{UV} at a value of ~ 0.6 . Moreover both Steidel *et al.* (1999) and Meurer *et al.* (1999) find for U -dropouts at $z \sim 3$ about the same median β of -1.6 (corresponding to $\alpha_{UV} = +0.6$) and deduce from this a median $E(B - V) \approx 0.15$ mag.

While this result was anticipated and is not a surprise, it is by no means one that is guaranteed. The mean starburst SED is not as blue as that of the hottest known stars, but rather represents a sum over a population including some very hot stars. There is no reason beyond our perception of what is logical why a very young galaxy could not have an even bluer UV SED, as do a very small number of local galaxies whose UV light may be dominated by the contribution of a few Wolf-Rayet stars (Sullivan *et al.* 2000, Brown *et al.* 2000). The bluest possible galaxy SED would be the Rayleigh-Jeans tail of a population of very hot stars, with $\alpha_{UV} = -2.0$, much bluer than that of observed galaxies. The mass of the highest mass star in a young population and the nature of the UV SED from a starbursts has been studied theoretically by Elmegreen (2000). He derives colors considerably bluer than observed starburst colors and is forced to introduce a mechanism to produce a cutoff in the upper mass below that expected.

We thus find strong evidence that the most extreme starburst galaxies (i.e. the bluest galaxies in the rest frame UV) have indistinguishable SEDs in the rest frame UV over the entire redshift range $0 < z < 3$.

⁶At $z > 1.2$, the 3727\AA emission line of [OII] is shifted to 8200\AA , where the night sky emission is becoming fierce. At $z > 1.5$, the line is shifted to the point where the quantum efficiency of most CCD detectors is rapidly declining.

⁷Ignoring the the starburst galaxy at $z = 0.137$, whose UV spectral index is not reliably determined, the five starbursts spectroscopically identified as such in our sample have a very wide range in α_{UV} from 0.1 to 2.7, with a very poorly determined median α_{UV} of 0.6.

5.2. On the Existence of Highly Reddened Starbursts in Our Sample

We now turn to the nature of the far IR objects observed in the sub-mm regime by SCUBA (Blain *et al.* 1999, Smail *et al.* 1999, Lilly *et al.* 1999, and for the HDF, Hughes *et al.* 1998), and their relationship to the galaxy populations normally studied at optical wavelengths. We use our SEDs to explore the issue of whether these galaxies might be some tail of the optically detected galaxy population with unusually high internal reddening. Smail *et al.* (1999), Richards (1999) and Barger, Cowie & Richards (2000), among others, have suggested that these far IR sources represent the tip of a vast iceberg of a separate population of very dusty galaxies at high z in which an enormous amount of star formation is occurring and which are invisible at optical wavelengths. Are these SCUBA sources closer to the ULIRGs reviewed by Sanders & Mirabel (1996) or to the redder of the Ly break galaxies already observed at optical wavelengths, as suggested by Adelberger & Steidel (2000) ? Do their presence and numbers imply that it is “useless” to study galaxies in the optical ?

Assuming SCUBA sources are not AGN but rather dusty starbursts, we attempt to isolate galaxies from our sample with a high rate of ongoing star formation most comparable to the galaxies detected with SCUBA. We take the group of galaxies with strong emission lines, i.e. those classified as \mathcal{E} as the relevant sample, recognizing that this is a somewhat more diverse group that may contain many galaxies “older” and with less current star formation than those detected by SCUBA or than pure local starburst galaxies. Hence the intrinsic UV power law index of many of these galaxies may be somewhat redder than that of a pure starburst.

Figure 8a suggests for strong emission line galaxies in our sample a continuous distribution of α_{UV} peaked at a level slightly redder than that of local starbursts and of $z \sim 3$ U -dropouts. There is no obvious second (redder) component, although there may be an extended low level red tail to the distribution. One should, however, note that the distribution in α_{UV} shown in figure 8a for the \mathcal{E} galaxies includes both \mathcal{E} and \mathcal{EI} galaxies.⁸ When restricted to just \mathcal{E} galaxies, the red tail is reduced relative to the blue peak. Furthermore, galaxies in the red tail of this distribution do not seem to have lower luminosities, as would be expected were the red tail due primarily to internal reddening.

This whole issue is related to the nature of the extremely red objects found in deep infrared selected samples. As we have stated earlier (Cohen *et al.* 1999a and Cohen *et al.* 2000), see also Scodreggio & Silva (2000), evidence from our redshift surveys suggests that the majority of the EROs in this magnitude regime with with $R - K \sim 5$ to 6 are passively evolving “old” stellar population at $z \sim 1.3$. While there are undoubtedly some very red very dusty ULIRGs and with extensive star formation similar to the ERO HR10 at $z = 1.44$ (Dey *et al.* 1999 and references therein), these appear to be rare.

⁸Unless otherwise specified, throughout this paper, a galaxy’s spectral class for purposes of plots and figures is defined only by the first character of its assigned spectral class.

Our analysis of the SEDs of galaxies with strong emission lines in our R -selected sample does not provide any evidence that supports the existence a significant “missed” population of dusty galaxies with extensive star formation which might be forming a significant fraction of the stars in the Universe within the regime $z \lesssim 1.5$. Dust enshrouded starburst nuclei which do not dominate the total integrated light from a distant galaxy cannot be excluded by our SEDs. However, Moriondo, Cimatti & Daddi (2000) and Stiavelli & Treu (2000) find that HST images of EROs are extremely red not just within the nucleus but over the entire galaxy image.

5.3. Prediction of the Mid-IR Flux from the UV Spectral Index

Meurer, Heckman, Calzetti (1999) have provided a formalism for predicting the far IR thermal dust emission from the UV spectral indices of starbursts. They suggest that as the amount of dust increases, the UV spectral index becomes redder and deviates further from the extremely blue power law index characteristic of bare young starbursts. The absorbed UV radiation is then re-emitted by dust in the mid and far infrared. Meurer *et al.* (1999) give the relevant relationships calibrated by their analysis of local starbursts to predict the emitted flux in the thermal IR from dust.

We attempt to use their formalism to predict which of the galaxies in the region of the HDF should have been detected in the mid-IR by ISO, assuming that a correlation between mid-IR and far-IR emission exists. We employ a ranking scheme to do this, comparing the list of galaxies actually detected by ISO from the analysis of Aussel *et al.* (1999) with our entire sample. The optical counterparts of the ISO galaxies are discussed and listed in Cohen *et al.* (2000). Only those with $R < 22.8$ (i.e. those for which the identification is considered reasonably certain) are included. Since the ISO optical counterparts are of spectral type \mathcal{E} , \mathcal{EI} or \mathcal{EA} (Cohen *et al.* 2000), we also predict the mid-IR flux for the galaxies within our sample of those spectral types (as well the the spectroscopically identified starbursts, which are mostly of too low luminosity to have been detected by ISO) and with $R < 22.8$.

Because of the correlation between galaxy spectral type and SED indices shown in Tables 2,3 and in Figure 8, a mis-classification of a galaxy to spectral type \mathcal{E} which is actually an intermediate spectral type (\mathcal{I} , \mathcal{EI} or \mathcal{IE}) will produce a galaxy that appears slightly too red in the rest frame UV, hence seems excessively dusty. The predicted mid-IR flux for such a mis-classified object will be overestimated. This type of classification error should not occur until a galaxy is either very faint or has $z > 0.9$, where the 4000Å region is shifted into the thicket of night sky lines and it is very hard to distinguish anything except the emission features. Hence the mid-IR luminosity prediction is carried out for the redshift range 0.25 to 1.05, omitting the highest z range, where the galaxy spectral types are more uncertain.

There are 12 ISO galaxies with secure optical counterparts in the relevant redshift range. We find the ranking of the 12 ISO galaxies in predicted mid-IR luminosity using the formalism

of Muerer *et al.* within the set of 154 potential optical counterparts from our survey selected as described above. For comparison, we ascertain the rank of the ISO galaxies in the total sample when ordered by $L(B)$ or by $L(R)$.

Figure 10 shows the rankings of the 12 ISO detected galaxies in this redshift range within the sample of 154 galaxies. A perfect discriminant would have the ISO galaxies occupying ranks 1 through 12. None of the discriminants tried is very good. The results are unchanged when only \mathcal{E} galaxies are used. They are also unchanged when a correction to the luminosity for passive evolution is made. The sBB SED model fits were used throughout; the results are unchanged when the 2p fits are used.

The best discriminant appears to be the B -band luminosity. The mid-IR flux predicted with the algorithm of Meurer *et al.* (1999) for the galaxies detected by ISO in our sample does not appear to do better overall than either the B or R band luminosity. While the ISO detections correspond to galaxies which are among the most luminous (using any of the three definitions of luminosity given above), there are still many galaxies of comparable luminosity that were not detected by ISO. The formalism of Meurer *et al.* (1999) does not significantly reduce this problem. One should note, however, that this formalism was developed to explain the far-IR emission of galaxies where thermal emission from dust dominates. At a typical redshift of 0.6, the 15μ ISO bandpass corresponds to 9.4μ in the rest frame. The majority of the ISO detections were in the 7μ band, where, in the rest frame for these distant galaxies, dust emission does not dominate the total emitted galaxy light.

6. Comments on Photometric Redshifts

Photometric redshifts have become very popular recently; see, for example, Connolly *et al.* (1997) or Fernandez-Soto, Lanzetta & Yahil (1999). As our blind tests (Hogg *et al.* 1998, Cohen *et al.* 2000) have shown, these are capable of accurately predicting the true redshift of an object in essentially all cases with the excellent photometry that one can obtain from deep HST images. But many wide area ground based surveys plan to use photometric redshifts for various purposes, and one might be concerned that the limitations of ground based photometry for such faint objects will reduce the accuracy of the resulting photometric redshifts beyond a tolerable level.

There are two problems here, both becoming worse as one presses fainter. The first is the impact of crowding while the second is the decreasing accuracy of the photometry itself for isolated fainter objects. We can assess the influence of the former in that even with very careful hand checking of all objects in our sample in the region of the HDF and with images with 1 arcsec seeing, we could not obtain believable SEDs for about 25 of 590 objects because of crowding.

⁹ Almost all of these objects have $R > 22$. That error rate in a massive non-manually checked

⁹The number of galaxies without reliable SEDs given in §3.8 includes galaxies with no observation at K as well

catalog at this magnitude level would be larger and would further increase by a large factor for a catalog with a fainter limiting magnitude or poorer seeing conditions. The influence of confusion on photometry is discussed by Hogg (2000). Even in the HDF itself, our survey still operates at a level in excess of 60 resolution elements per source.

The 4000Å break is the dominant feature in the spectra of galaxies in this redshift range.¹⁰ If the photometric errors are such that it is impossible to discern the presence of the break, assignment of a photo- z becomes problematic at best.

We can test with each of our two fitting models whether a 4000 Å break is measurable. In the case of the 2p SED model, we require that we can detect $\alpha_{IR} - \alpha_{UV}$, which is a broad band change in continuum slope, as non-zero, while the sBB model permits direct measurement of the 4000 Å break.

Our criterion for detectability for the 4000 Å break in the sBB SED model is that $L(\lambda_m, \text{red}) - L(\lambda_m, \text{blue}) \geq 0.05$ dex (corresponding to a 4000 Å break of ≥ 0.13 mag). For the 2p model, we require that $|(\alpha_{IR} - \alpha_{UV})|/\sigma \geq 1.5$, where σ is determined from the fitting procedure and is based on the observed brightness of the object, the number of filters used to determine the SED, and the redshift of the object.

We find the number of galaxies in each redshift range for which, with the definitions given above, the detection of a 4000 Å break is problematical. This fraction is less than 20% for galaxies with $z < 0.8$, but rises to more than 30% above $z \sim 0.8$. While the overall fraction of galaxies without detectable 4000 Å breaks is approximately the same for the two SED models, the behavior of galaxies of spectral class \mathcal{A} , in particular, depends on the fitting scheme adopted. In the 2p model, essentially all such galaxies have easily detectable breaks, while in the more detailed sBB model, they have small 4000 Å break, but still display substantial changes in overall spectral slope between the rest frame UV and optical. In any case, there is clearly a significant population of galaxies, consisting predominantly of those with strong emission lines, that do not have a detectable 4000Å break or Balmer jump. For such galaxies, adding IR photometry will not help in providing a valid photometric redshift. Only higher precision photometry, difficult to achieve from the ground for such faint objects, will help.

Brunner, Szalay & Connolly (2000) have discussed this issue at length as it affects their study of galaxy clustering, which uses photometric redshifts to divide a pencil beam survey into several redshift shells, thus avoiding the projection integral. Their particular application is eased by the fact that, as shown by Hogg, Cohen & Blandford (2000), throughout this range in z most of the clustering signal is from the redder early type galaxies, which will yield reasonably accurate photo- z s under any appropriate scheme.

as those suffering from crowding.

¹⁰We ignore the higher redshift range where the Ly break dominates and where the decline in flux across the boundary is more than a factor of 10, but the objects are in general fainter than the range considered here of $R < 24$.

7. A Qualitative View of the Evolution of $L^*(K)$

We show in Figure 11 the rest frame K -band luminosity $L(K)$ calculated from the sBB parameters of the SED fits as a function of cosmological comoving volume. The issue of K -corrections has been avoided through the use of multi-color photometry spanning a broad wavelength range. However, extrapolation beyond the reddest observations (i.e. trusting the functional form of the model SEDs) is required to obtain rest frame K magnitudes for galaxies in this sample, with the largest extrapolation required for the highest z galaxies.

The rationale for studying galaxies at K is that the integrated light there is much more representative of the total stellar mass of a galaxy than are the optical colors, where light from the most recent epoch of star formation may dominate over that from the older population as one moves towards the ultraviolet. To convert these K luminosities for the galaxies in our sample into total stellar masses of the galaxies requires a model of evolving galaxy spectral energy distributions to evaluate their mass-to-light ratio as a function of look back time and of their star formation history. We use the evolutionary corrections from the models of Poggianti (1997), and interpret her E, Sa and Sc galaxy classes as roughly equivalent to our galaxy spectral types \mathcal{A} , \mathcal{I} and \mathcal{E} . The lines in Figure 11 thus indicate the predicted track of a galaxy of constant mass from Poggianti for the three morphological galaxy classes. As expected, the evolutionary change in luminosity at K predicted by Poggianti is quite small and much less dependent on the details of the star formation history (i.e. of the galaxy spectral class) than are those predicted at B or R . These tracks, which include passive stellar evolution for the elliptical, are at rest frame K a good representation of the evolution of at least the most luminous galaxies in our sample.

Recent determinations of $L^*(K)$ in the local Universe correspond to $L^*(K) = 8 \times 10^{36}$ W (Gardner *et al.* 1997, Loveday 1999, and from the combination of the 2dF and 2MASS survey, Cole *et al.* 2000). The passive evolution model lines are shown with this luminosity (at $z = 0$), equivalent to $1.3 \times 10^{11} L_{\odot}$ at K . For elliptical galaxies, using the mass-to-light ratio at K for local ellipticals computed by Worthey (1994), this is a galaxy with a total mass of $1 \times 10^{11} M_{\odot}$. The mass-to-light ratio of Sb galaxies is smaller, by about a factor of 2.

Figure 11 suggests, as has been evident from our work on spatial clustering in this field, that luminous nearby ($z \lesssim 0.3$) galaxies are absent in this field. That is presumably a result of the selection criteria for defining the HDF adopted by Williams *et al.* (1996).

Figure 11 also shows the gradual increasing mean luminosity of star forming galaxies (our spectral class \mathcal{E}) to $z \sim 1$, and the increasing dominance of such galaxies as a fraction of the total observed population, an effect found previously with smaller samples by many groups, including Cowie *et al.* (1996), Hammer *et al.* (1997) and Hogg *et al.* (1998). There are some selection effects, as discussed many times in the earlier papers in this series, namely faint objects have a lower probability of being assigned a redshift unless they have very strong emission lines and the same is true for galaxies with $z > 1$. However, the redshift completeness of our sample is very high, in excess of 93%.

A formal analysis of the galaxy luminosity functions will follow in the next paper in this series. Once the evolution of L^* is properly determined, then subject to the accuracy of Poggianti’s (1997) predicted evolutionary corrections at rest frame K and to the uncertainties in the extrapolation of our SEDs beyond the range in wavelength over which photometry exists, one can evaluate the change in the total stellar mass of L^* galaxies. This can then be used to provide another constraint on the rate of massive mergers out to $z \sim 1$; Carlberg *et al.* (2000) has already provided one such constraint through an analysis of the kinematic pairs in our sample.

8. Summary

In this paper we have evaluated the spectral energy distributions for a sample of 590 galaxies in the region of the HDF with $z < 1.5$ using a new versatile and stable SED model. This has been done directly from the data using multi-color photometry with wide wavelength coverage combined with spectroscopic redshifts from our 93% complete R -selected redshift survey here. The behavior of the SEDs with galaxy spectral type (i.e. “recent” star formation history) and with redshift confirms the trends found in our earlier studies of smaller samples; galaxies with strong signs of recent star formation (i.e. those which show emission lines) have bluer continuum slopes in both the rest frame UV and the optical/near-infrared. The most luminous galaxies tend to be of galaxy spectral class \mathcal{A} at a rate much higher than their fraction in the total sample, i.e. the redder galaxies tend to be more luminous. In the mean, actively star forming galaxies become bluer in the rest-frame UV at higher redshifts, which may perhaps be due to systematic redshift dependent fitting errors for $\alpha(UV)$. We see no other change with redshift in the relationship between SED characteristics and galaxy spectral type defined by the presence and strength of narrow emission and absorption features to $z \sim 1.1$.

We use these SEDs to evaluate the potential accuracy of photometric redshifts, bearing in mind that a break at 4000\AA must be detectable to within the errors of the photometry to assign a photo- z for galaxies in this redshift regime. We also use them to demonstrate that the SEDs in the rest frame UV of the the most extreme starburst galaxies (i.e. the bluest \mathcal{E} galaxies) are indistinguishable SEDs from those of local starbursts as analyzed by Calzetti, Kinney & Storchi-Bergmann (1994) and from those of the Ly break galaxies at $z \sim 3$ studied by Steidel *et al.* (1999) and by Meurer *et al.* (1999).

We also attempt to set constraints on the possible existence of a separate class of dusty starburst galaxies and on the variation from galaxy to galaxy within a galaxy spectral class of internal reddening using these SED indices. Finally we use the UV spectral indices of all the strong emission line galaxies to predict which of them should have been detected by ISO in the mid-IR, which exercise was only modestly successful.

We conclude by presenting the rest frame K -band luminosity as a function of z . We see the effect of selecting a field (i.e. the HDF) to be devoid of bright galaxies. We see encouraging

overall consistency with predictions of evolutionary corrections for the rest frame $L(K)$ computed from models of integrated light of galaxies by Poggianti (1997). We see the gradual change in the population of various types of galaxies, with star forming galaxies becoming both a larger fraction of the total population and more luminous as one moves toward $z \sim 1$. The overall pattern of the $L(K) - z$ relationship suggests that passive evolution at constant total stellar mass is a good approximation to the actual behavior of at least the most luminous galaxies in this large sample of galaxies in the region of the HDF out to $z \sim 1.5$, an issue which will be explored in depth in the next paper in this series.

The entire Keck/LRIS user community owes a huge debt to Jerry Nelson, Gerry Smith, Bev Oke, and many other people who have worked to make the Keck Telescope and LRIS a reality. We are grateful to the W. M. Keck Foundation, and particularly its late president, Howard Keck, for the vision to fund the construction of the W. M. Keck Observatory.

We thank Roger Blandford, David Hogg and Gerry Neugebauer for helpful discussions. We thank Amy Barger and Len Cowie for access to their unpublished photometric database for the region of the HDF. We thank Robert Brunner for supplying filter transmission curves. We thank two anonymous referees for constructive criticism of the manuscript.

This work was not supported by any federal agency.

A. Updates to the Redshift Catalog in the Region of the HDF

We present in Tables 6a,b redshifts obtained since November 1999 for objects in the region of the HDF. This is new, additional material which supplements that presented in Cohen *et al.* (2000). The galaxy spectral classes and redshift quality classes used here are those defined in Cohen *et al.* (1999a). Table 6a contains information for 53 objects in the Flanking Fields and is based exclusively on our LRIS (Oke *et al.* 1995) observations at the Keck Observatory during the winter of 2000. Emphasis in planning the observations was on galaxies with $23.0 < R < 23.5$.

Table 6b contains the additional redshifts for five objects in the HDF itself, some of which is from other groups as indicated in the table.

Combining this new material with the data presented in Cohen *et al.* (2000), the redshift completeness in the HDF itself to $R < 24$ is now 95%, while that in the Flanking Fields around to within the survey area of Cohen *et al.* is in excess of 93% to $R < 23$.

The SED parameters for these new galaxies with $z < 1.5$ for which reliable SEDs are given in Table 7a,b.

In addition, three redshifts from the catalog of Cohen *et al.* (2000) are being changed. The spectral features which led to the redshift assignment given in our catalog in each case are real, but

the identification assigned to them has been modified. Based on a suggestion from Mark Dickinson (private communication), the same suggestion subsequently being made by Fernandez-Soto *et al.* (2000), and after looking at the relevant spectra, the redshift of H36396_1230 has been changed. What in hindsight should have been recognized as an obvious Ly α emission line was previously identified as the Mg II line at 2800Å. The redshifts of H36494_1316 and H36560_1329 are also being modified to identify the single emission line as [OII] 3727Å instead of H α to be in conformance with the rules stated in earlier papers in this series regarding redshifts from spectra showing only single emission lines and also based on the photometric redshift/spectroscopic redshift discrepancy discussed by Fernandez-Soto *et al.*. If these rules had been followed in all 3 cases, no modifications would have been necessary. The corrections are listed in Table 8. The SEDs have been calculated using the updated values.

Finally, the magnitude given for H36453_1153 in Cohen *et al.* (2000) is too bright. There are several faint objects close together which are clearly resolved in the HST image, but only one entry appears in the H00 photometric catalog. The object with the spectroscopic redshift is the *U*-dropout, and instead of $R = 22.53$, the value given in Cohen *et al.* (2000), a better estimate for this galaxy is $R \sim 23.3$.

B. Effective Wavelengths of the Filters

The effective wavelength of the K_s (short K) filter is taken as 2.17μ with an absolute flux at 0 mag of $\log[\nu f_\nu] = -9.01 \text{ W m}^{-2}$ (M.Pahre, private communication). Persson *et al.* (1998) also discuss the effective wavelengths of various infrared photometric systems. The effective wavelengths of the other three filters in the H00 database (U_n , G_n and R) are given by Steidel & Hamilton (1993). The Barger *et al.* (1998) database consists of at least six colors, five of which are on the Johnson system, and hence their effective wavelengths can be taken from standard sources; we adopt those of Fukugita, Shimasaku & Ichikawa (1995). The notched HK' filter is described in Barger *et al.* (1998); see also Wainscoat & Cowie (1992). The galaxy measurements at HK' were transformed to a standard Johnson K using the relationship $K = HK' - 0.3$ given by Barger *et al.* (1998).

C. Details of the SED Fitting Procedures

Here we describe the details of the fitting procedures, and how the flux at the transition wavelength is handled.

For the 2p SED, the power law was fit first to the side (blue or red) of rest frame 4000Å which had the most observed points; this depended on the redshift of the object and the number of filters for which data actually exists. A linear least squares fitting routine from Press *et al.* (1986) was used. Once one index was determined, the second spectral index is calculated assuming forced

agreement in the value of L_ν at 4000\AA .

For the sBB SED model, the fitting is accomplished with routines from Press *et al.*(1986). The fitting rules are as follows. If there are 4 or more filter bands observed on the red side and 3 or more on the blue side, then the regimes $\lambda < \lambda_m$ and $\lambda > \lambda_m$ are fit independently. If there are fewer than four on the red side, then the blue side is fit first. A point is then added to the red side at λ_m with the luminosity there that calculated from the blue fit. Then the red fit is done. If there are fewer than three on the blue side, then the red side fit is done first, and a point is added to the blue side at λ_m with the value predicted from the sBB fit.

REFERENCES

- Aaronson, M., 1978, ApJ, 221, 103
- Adelberger, K. & Steidel, C. C., 2000, ApJ, 544, 218
- Aussel, H., Cesarsky, C.J., Elbaz, D. & Starck, J.L., 1999, A&A, 342, 313
- Barger, A. J., Cowie, L. L., Trentham, N., Fulton, E., Hu, E. M., Songaila, A. & Hall, D., 1998, AJ, 117, 102
- Barger, A. J., Cowie, L. L. & Richards, E. A., 2000, AJ, 119, 2092
- Bertin, E. & Arnouts, S., 1996, A&AS, 117, 393
- Blain, A. W., Kneib, J. P., Ivison, R. J. & Smail, I., 1999, ApJ, 512, L87
- Blanton, M. R. *et al.*, 2000, AJ (submitted) (astro-ph/0012085)
- Boselli, A., Gavazzi, G., Donas, J. & Scodreggio, M., 2000, A&A (in press), astro-ph/0011016
- Brown, W. R., Kenyon, S. J., Geller, M. J. & Fabricant, D. G., 2000, ApJ, 540, L83
- Brunner, R. J., Szalay, A. S. & Connolly, A. J., 2000, ApJ, 541, 527
- Budavári, T., Szalay, A.S., Connolly, A.J., Csabai, I. & Dickinson, M., 2000, AJ, 120, 1588
- Calzetti, D., 1997, AJ, 113, 162
- Calzetti, D., Kinney, A. L. & Storchi-Bergmann, T., 1994, ApJ, 429, 582
- Carlberg, R. G., Cohen, J. G., Patton, D. R., *et al.* 2000, ApJ, 532, L1
- Moriondo, G., Cimatti, A. & Daddi, E., 2000, A&A, in press (astro-ph/0010335)
- Cohen, J. G., Blandford, R., Hogg, D. W., Pahre, M. A. & Shopbell, P. L., 1999a, ApJ, 512, 30
- Cohen, J. G., Hogg, D. W., Pahre, M. A., Blandford, R., Shopbell, P. L. & Richberg, K., 1999b, ApJS, 120, 171
- Cohen, J. G., Hogg, D. W., Blandford, R., Cowie, L. L., Hu, E., Songaila, A., Shopbell, P. & Richberg, K., 2000, ApJ, 538, 29
- Cole, S. *et al.*, 2001, MNRAS, in press (astro-ph/0012429)
- Coleman, G. D., Wu. C. C. & Weedman, D. W., 1980, ApJS, 43, 393
- Connolly, A. J., Szalay, A. S., Dickinson, M., SubbaRao, M. U. & Brunner, R. J., 1997, ApJ, 486, L11
- Côté, P., Oke, J.B. & Cohen, J.G., 1999, AJ, 118, 1645
- Cowie, L. L., Songaila, A., Hu, E. M. & Cohen, J. G., 1996, AJ, 112, 839
- Dey, A., Graham, J. R., Ivison, R. J., Smail, I., Wright, G. S. & Liu, M. C., 1999, ApJ, 519, 610
- Dickinson, M. E., 2000, in *Building Galaxies: From the Primordial Universe to the Present*, XIXth Moriond Astrophysical Meeting, eds. Hammer, F. *et al.*, (Paris: Ed. Frontievers), p257 (astro-ph/0004027)

- Ellis, R. S., Colless, M., Broadhurst, T., Heyl, J. & Glazebrook, K., 1996, MNRAS, 280, 235
- Elmegreen, B.G., 2000, ApJ, 539, 342
- Fernandez-Soto, A., Lanzetta, K. M. & Yahil, A., 1999, ApJ, 513, 34
- Fernandez-Soto, A., Lanzetta, K.M., Chen, H.W., Pascarelle, S. & Yahata, N., 2000, astro-ph/0007447
- Folkes, S. *et al.* 1999, MNRAS, 308, 459
- Frogel, J. A., Persson, S. E., Aaronson, M. & Matthews, K., 1978, ApJ, 220, 75
- Fukugita, J., Shimasaku, K. & Ichikawa, T., 1995, PASP, 107, 945
- Gardner, J. P., Sharples, R. M., Frenk, C. S., Carrasco, B. E. 1997, ApJ, 480, L99
- Hammer, F., Flores, H., Lilly, S. J., Crampton, D., Le Fèvre, O., Rola, C., Mallen-Ornelas, G., Schade, D. & Tresse, L., 1997, ApJ, 481, 49
- Hogg, D. W., Cohen J. G. & Blandford R., 2000, ApJ, 545, 32
- Hogg, D. W., Cohen J. G., Blandford R., Gwyn S. D. J., Hartwick F. D. A., Mobasher B., Mazzei P., Sawicki M., Lin H., Yee H. K. C., Connolly A. J., Brunner R. J., Csabai I., Dickinson M., SubbaRao M. U. & Szalay A. S., 1998, AJ, 115, 1418
- Hogg, D. W., Cohen J. G., Blandford R. & Pahre, M. A., 1998, ApJ, 498, L59
- Hogg, D. W., Neugebauer, G., Cohen, J. G., Dickinson, M., Djorgovski, S. G., Matthews, K. & Soifer, B. T., 2000, AJ, 119, 1519
- Hogg D. W., 2000, AJ, submitted (astro-ph/0004054)
- Hogg D. W., Pahre M. A., Adelberger K. L., Blandford R., Cohen J. G., Gautier T. N., Jarrett T., Neugebauer G. & Steidel C. C., 2000, ApJS, 127, 1 (H00)
- Hornschemeier, A. E., *et al.* 2000, ApJ, 541, 49
- Hughes, D., *et al.*, 1998, Nature, 394, 241
- Lilly, S. J., Eales, S. A., Gear, W. K. P., Hammer, F., Le Fèvre, O., Crampton, D., Bond, J. R. & Dunne, L., 1999, ApJ, 518, 641
- Lin, H., Kirshner, R. P., Sheckman, S. A., Landy, S. D., Oemler, A. & Shechter, P. L., 1996, ApJ, 464, 60
- Loveday, J., 2000, MNRAS, 312, 557
- Meurer, G. R., Heckman, T. & Calzetti, D., 1999, ApJ, 521, 64
- Oke, J. B., Cohen, J. G., Carr, M., Cromer, J., Dingizian, A., Harris, F. H., Labrecque, S., Lucinio, R., Schaal, W., Epps, H., & Miller, J. 1995, PASP, 107, 307
- Persson, S. E., Murphy, D. C., Krzeminsky, W., Roth, M. & Rieke, M. J., 1998, AJ, 116, 2475
- Poggianti, B. M., 1997, A&A Supl, 122, 399

- Press, W.H., Flannery, B.P., Teukolsky, S.A. & Vetterline, W.T., 1986, Numerical Recipes, Cambridge University Press
- Richards, E. A., 2000, ApJ, 533, 611
- Richards, E. A., Fomalont, E. B., Kellerman, K. I., Windhorst, R. A. & Partridge, R. B., 1998, AJ, 116, 1039
- Richards, E. A., Fomalont, E. B., Kellerman, K. I., Windhorst, R. A., Partridge, R. B., Cowie, L. L. & Barger, A. J., 1999, ApJ, 526 L73
- Sanders, D. B. & Mirabel, F., 1996, ARA&A, 34, 749
- Scodreggio, M. & Silva, D., 2000, A&A, 359, 953
- Schlegel, D. J., Finkbeiner, D. P. & Davis, M., 1998, ApJ, 500, 525
- Smail, I., Ivison, R. J., Kneib, J. P., Cowie, L. L., Blain, A. W., Barger, A. J., Owen, F. N. & Morrison, G., 1999, MNRAS, 308, 1061
- Steidel, C.C. & Hamilton, D., 1993, AJ, 105, 2017
- Steidel, C.C., Adleberger, K. L., Giavalesco, M., Dickinson, M. & Pettini, M., 1999, ApJ, 519, 1
- Stern, D. & Spinrad, H., 1999, PASP, 111, 1475
- Stiavelli, M. & Treu, T., 2000, to appear in “Galaxy Disks and Disk Galaxies”, ASP Conf. Series (astro-ph/0010100)
- Sullivan, M., Treyer, M.A., Ellis, R.S., Bridges, T.J., Milliard, B. & Donas, J., 2000, 312, 442
- van den Bergh, S., Cohen, J. G., Hogg, D. W. & Blandford, R., 2000, AJ, 120, 2190
- Wainscoat, R. J. & Cowie, L. L., 1992, AJ, 103, 332
- Williams, R. E., *et al.* 1996, AJ, 112, 1335
- Worthey, G. W., 1994, ApJS, 95, 107
- Zaritsky, D., Kennicutt, R.C.Jr & Huchra, J.P., 1994, ApJ, 420, 87

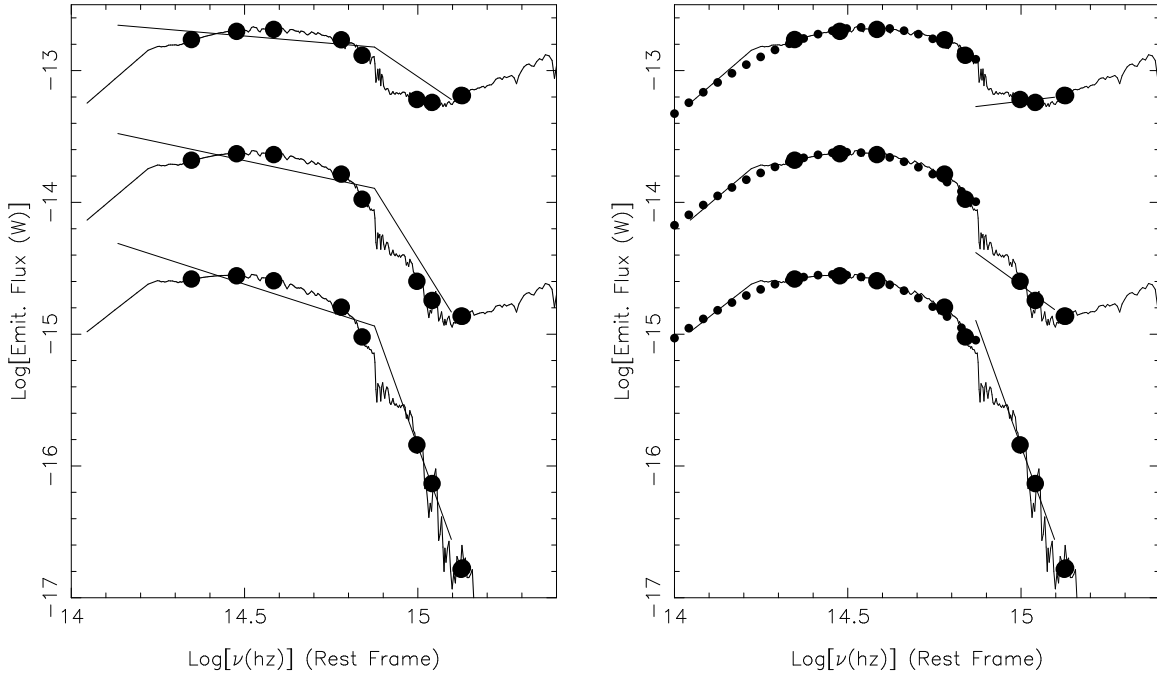


Fig. 1.— a) The SEDs of $z = 0$ elliptical, Sa and Sc galaxies from Poggianti (1997), shown as the curves, are observed at a redshift of 0.6. The resulting filter bands are indicated by the large filled circles. The 2p SED model is then fit to this set of filter data and the UV and IR fit for each of the three SEDs is shown as a straight line. b) The same as Figure 1a, but using the sBB SED model. The best fit is shown as the small filled circles for the sBB function and as the solid line for the power law in the UV.

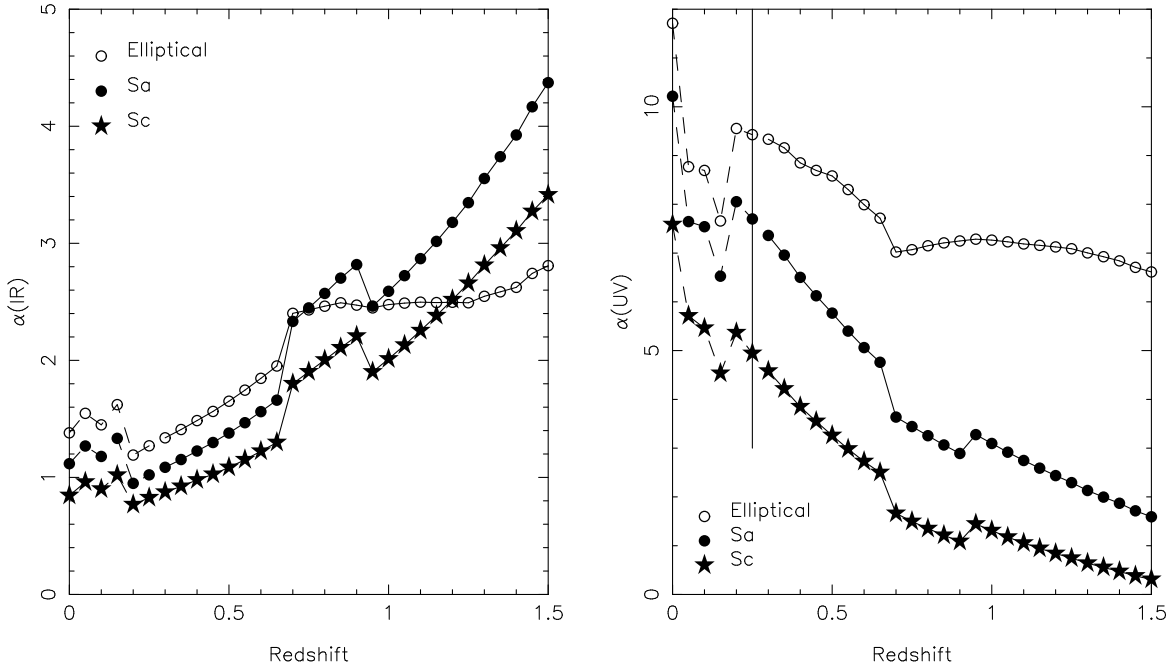


Fig. 2.— The UV and IR power law indices found from the 2p model of galaxy SEDs are shown for the standard test set of local SEDs (those of Figure 1). The redshift of observation ranged from $z = 0.0$ to 1.5. Open circles denote the track of the SED parameters determined for the local elliptical galaxy SED, filled circles show that of a local Sa, and stars the local Sc galaxy. The vertical line in panel (a) reminds us that the UV fit is not considered valid in the region $z < 0.25$.

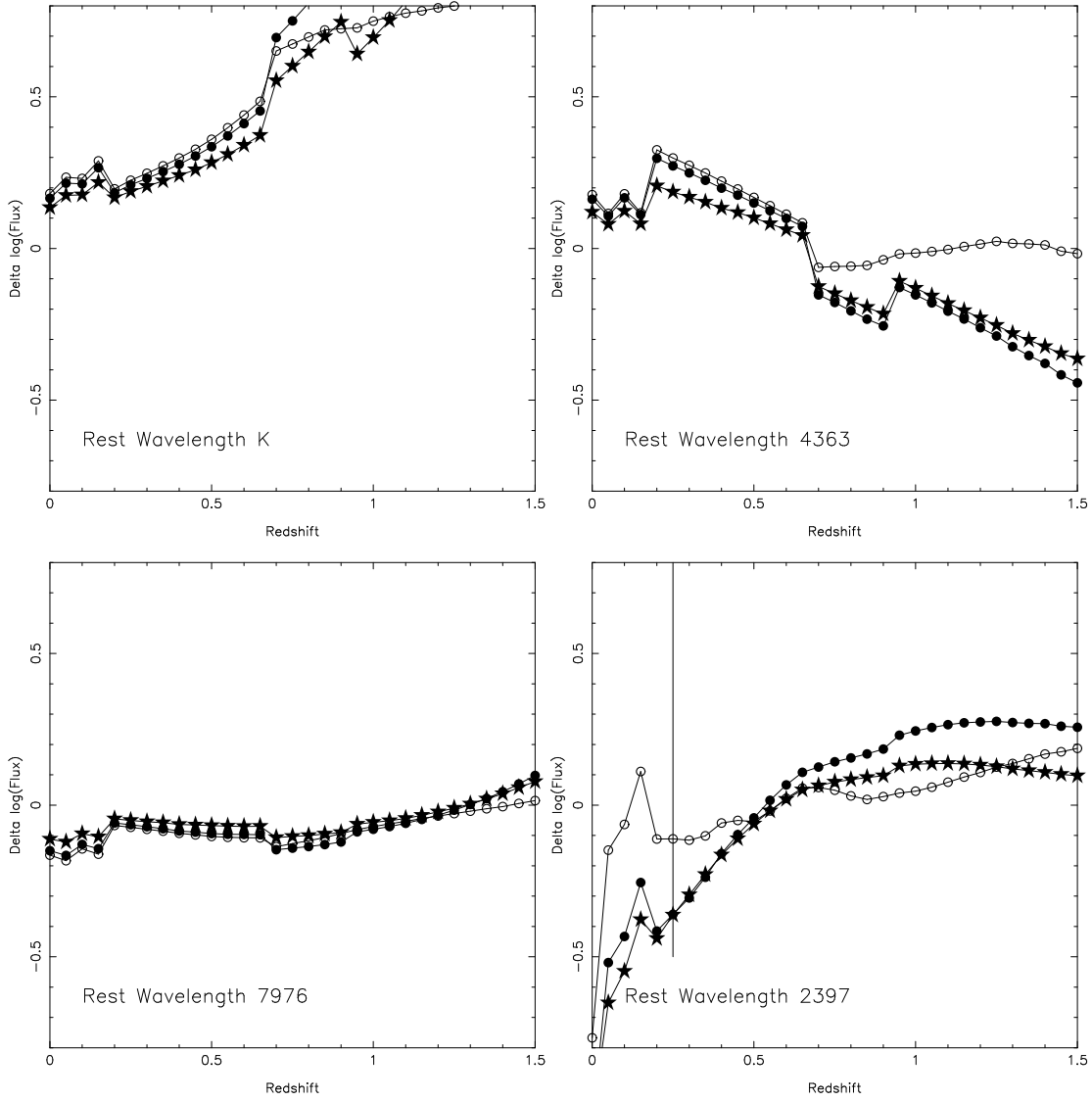


Fig. 3.— The rest frame galaxy luminosity $L(\nu_0)$ predicted by the best fit 2p SED model is compared with the actual luminosity of the standard test set of local galaxy SEDs, which are observed over the range in redshift from 0 to 1.5. The plot symbols are the same as those of figure 2. The four panels give the results for four different rest wavelengths.

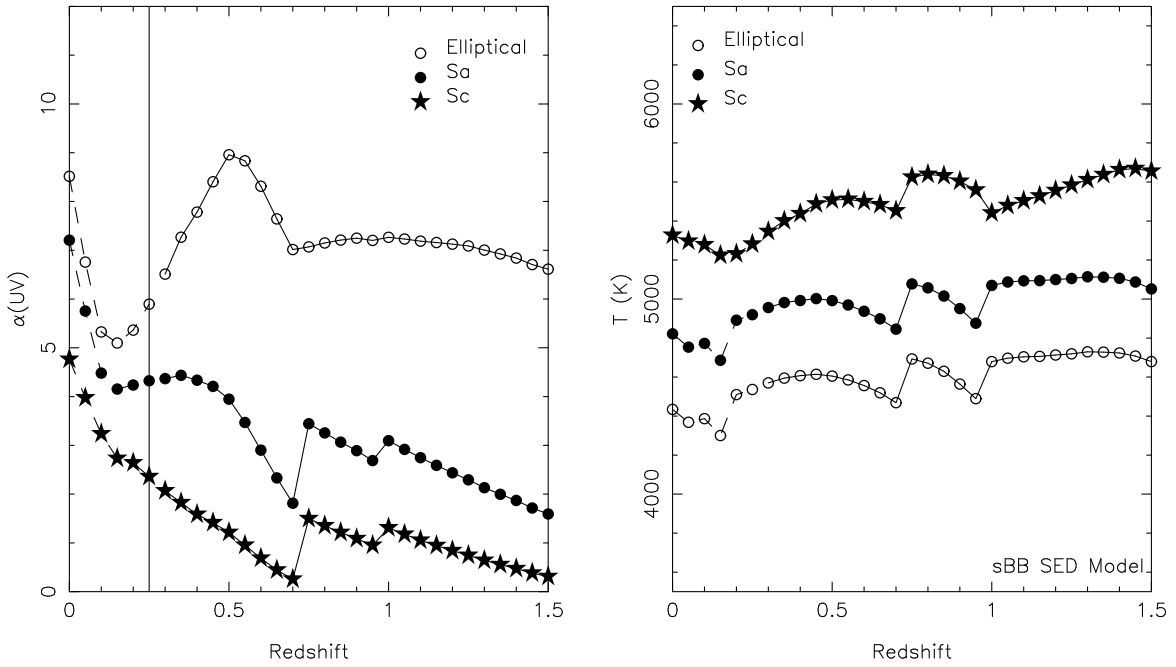


Fig. 4.— The measured parameters from the sBB model fit are shown (α_{UV} in (a) and T for the optical and near IR in (b)) for the standard test set of local galaxy SEDs (those of Figure 1) observed over the range in redshift from 0.0 to 1.5. The plot symbols are the same as those of figure 2. The vertical line in panel (a) reminds us that the UV fit is not considered valid in the region $z < 0.25$.

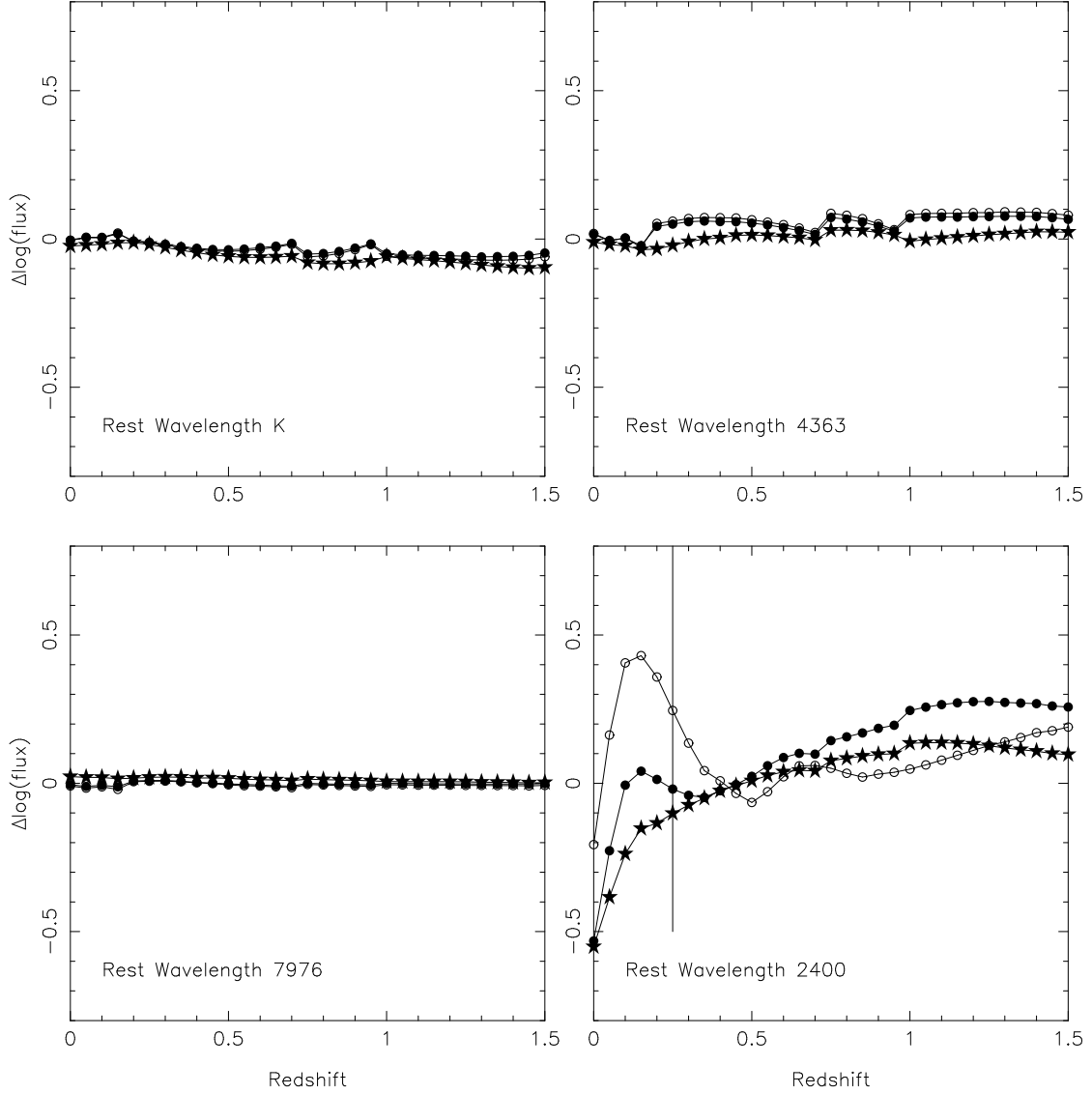


Fig. 5.— The rest frame galaxy luminosity $L(\nu_0)$ predicted by the best fit sBB SED model is compared with the actual luminosity of the galaxy SED for the set of standard local galaxy SED models observed over the range in redshift from 0 to 1.5. The plot symbols are the same as those of figure 3. The four panels give the results for four different rest wavelengths and are identical in wavelength and scale to the panels of Figure 3.

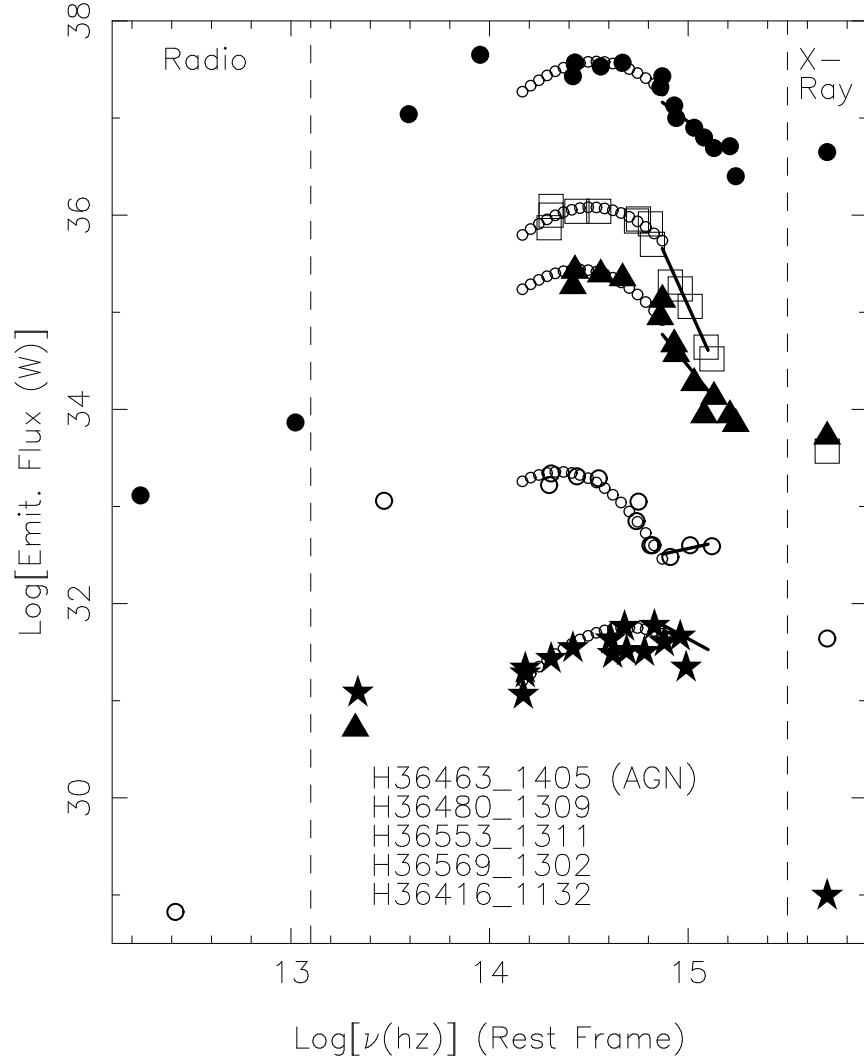


Fig. 6.— The SEDs for the five galaxies in the HDF in our sample with detections in the X-ray by Chandra from Hornschemeir *et al.* (2000) included. The sBB fits are shown as well as the mid-IR detections from ISO from Aussel *et al.* (1999) and the VLA radio detections of Richards *et al.* (1998) and Richards (2000) at 1.4 and 8.5 GHz. The frequency scale is correct for the optical and mid-IR, but is discontinuous at each end to include the radio and X-ray detections. The vertical scale is correct for the uppermost galaxy (H36463_1405) shown. A vertical shift of 1 dex downward is applied for each additional galaxy plotted. The vertical order of the galaxies in the optical is that given in the text insert at the bottom of the figure.

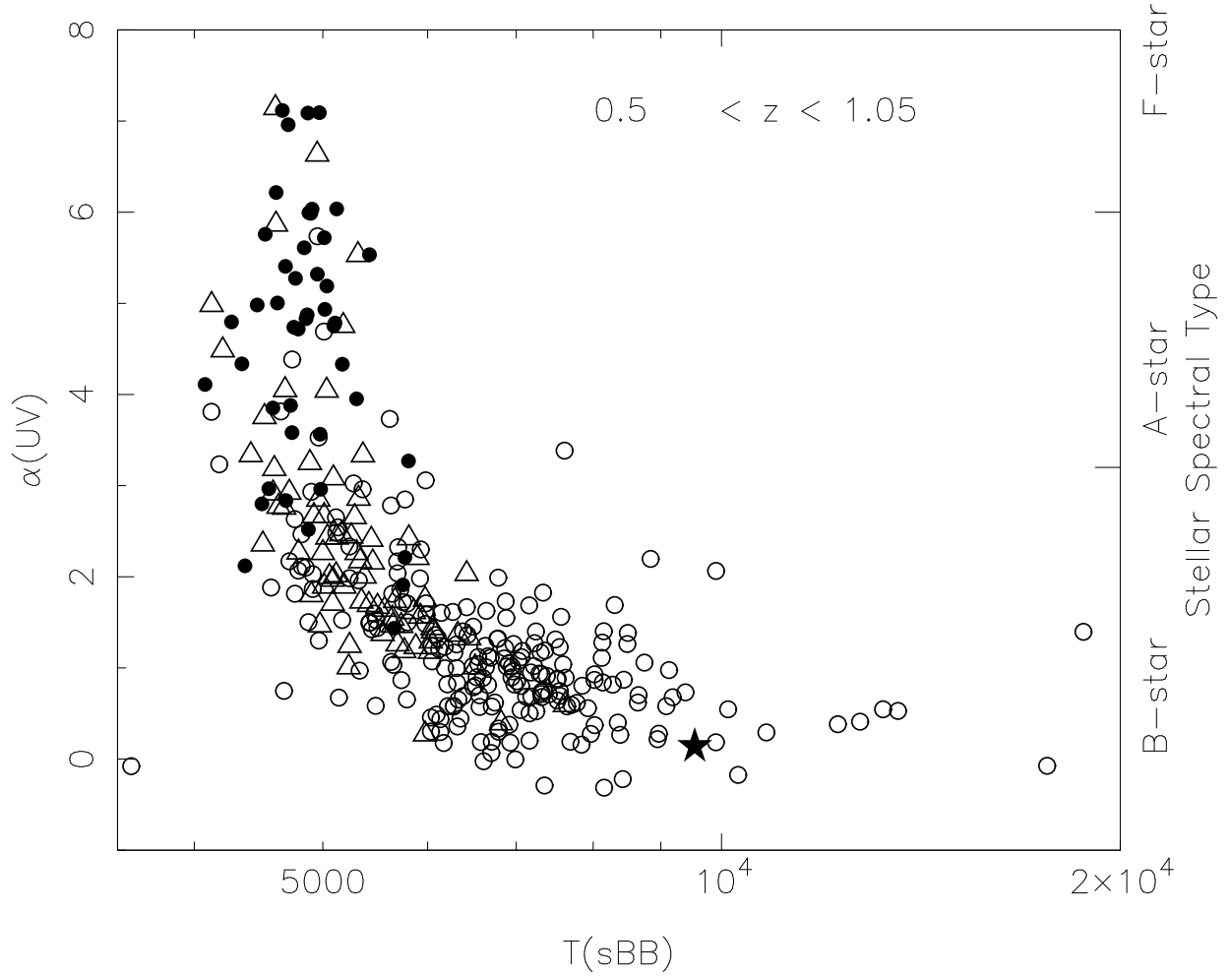


Fig. 7.— The spectral indices α_{UV} are shown as a function of $\log(T)$ for galaxies in the region of the HDF in the “mid” and “high” redshift ranges. Filled circles denote galaxies of spectral type \mathcal{A} , triangles denote galaxies of spectral type \mathcal{I} , and open circles denote galaxies with strong emission lines (spectral type \mathcal{E}). Starbursts (spectral type \mathcal{B}) are denoted by stars. Note that only the first letter of the galaxy spectral class is used. The range of α_{UV} for stars of various spectral types, taken from Cohen *et al.* (1998a), is shown on the right side of the figure.

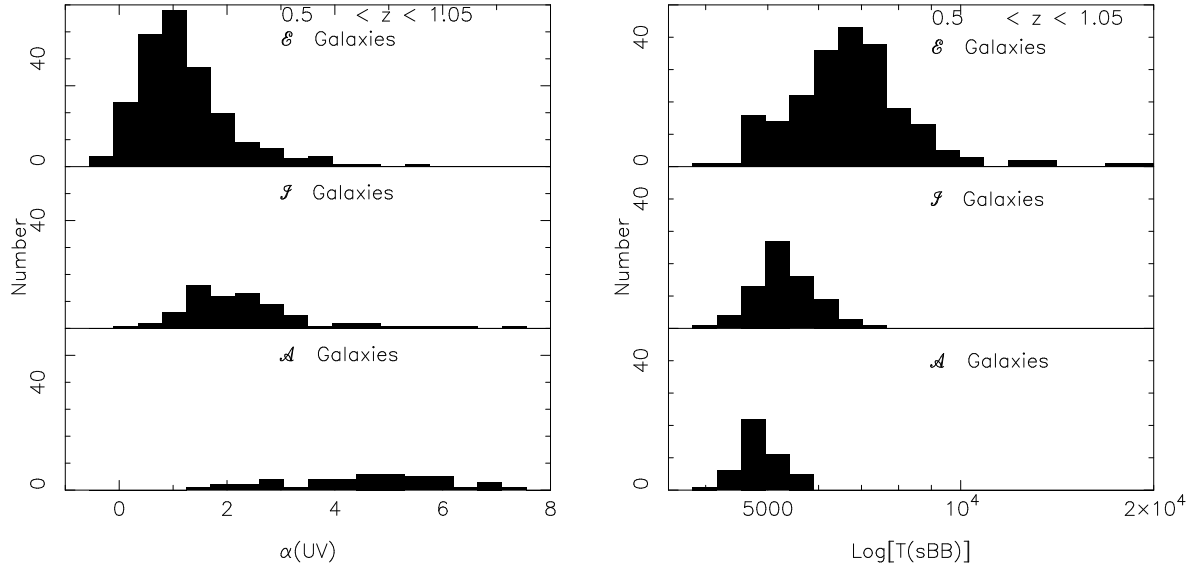


Fig. 8.— Histograms of the the spectral indices α_{UV} and $T(sBB)$ are shown in Figures 8a and 8b for galaxies of spectral classes \mathcal{A} , \mathcal{I} and \mathcal{E} in the “mid” and “high” redshift ranges. Note that only the first letter of the galaxy spectral class is used.

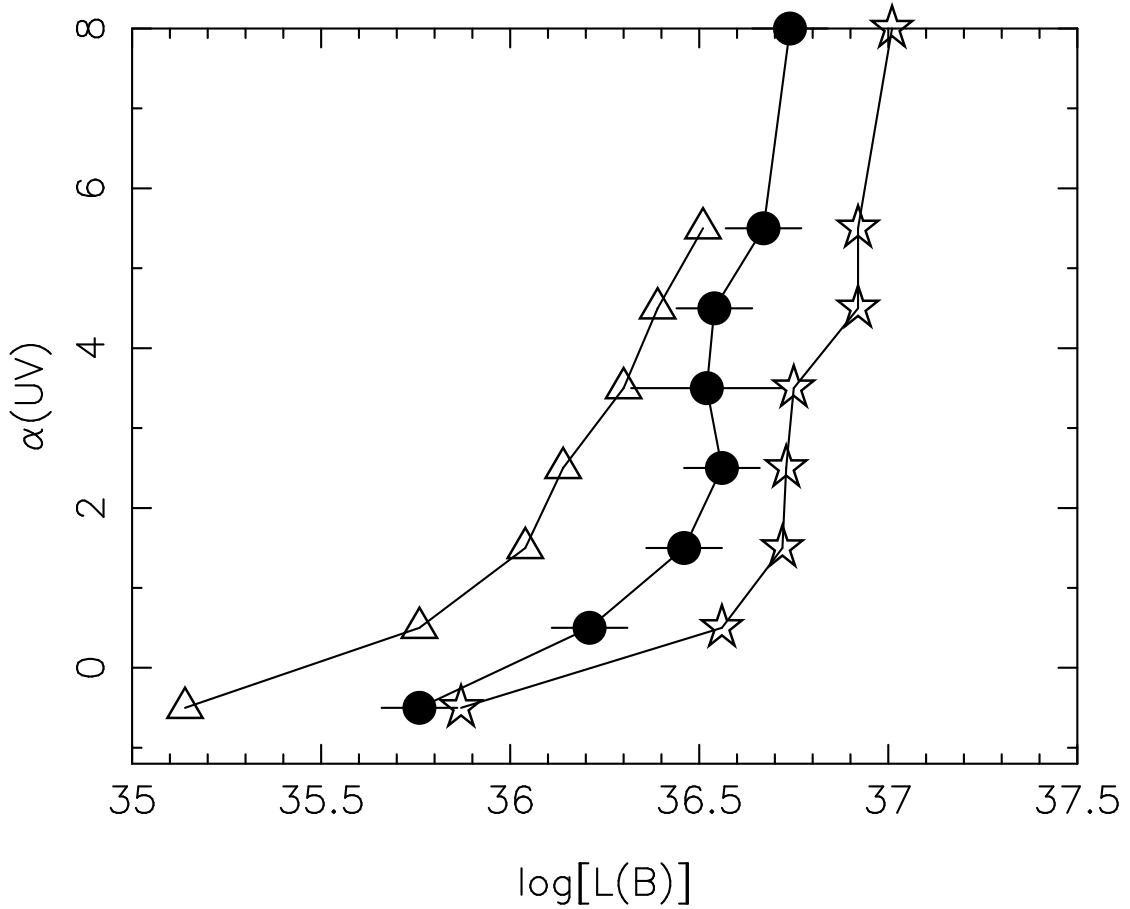


Fig. 9.— The relationship between the median luminosity $L(B)$ in bins of rest frame UV spectral slope $\alpha(UV)$ is shown as a function of redshift for three of the four redshift bins. (The highest redshift bin is not shown.) The open triangles denote the sample of galaxies in the region of the HDF with $0.25 < z < 0.5$, the filled circles denote galaxies with $0.5 < z < 0.8$, and the stars denote galaxies with $0.9 < z < 1.05$. The range in luminosity within a given bin in UV spectral slope is indicated by the $\pm 1\sigma$ horizontal bars displayed for the second redshift range only. More luminous galaxies are seen to be redder in the rest frame UV.

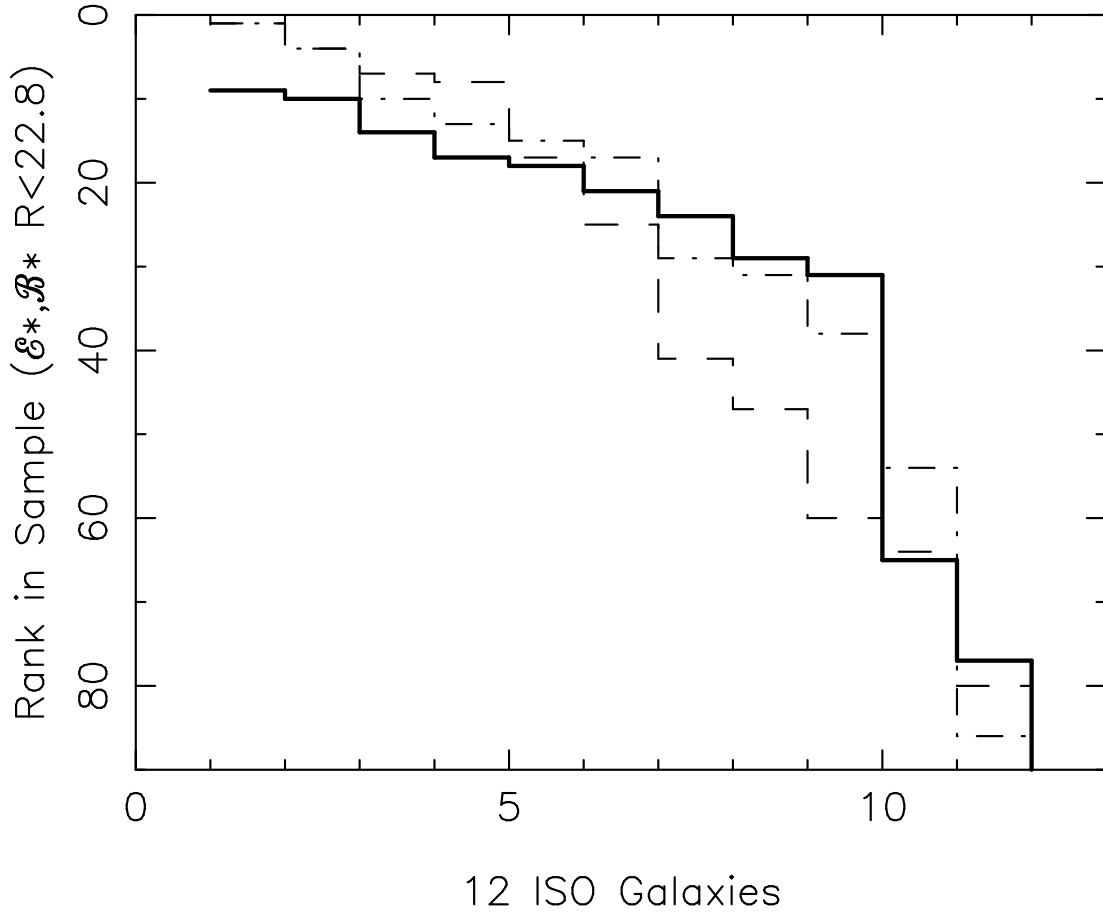


Fig. 10.— The ranking of the galaxies detected by ISO within the sample of all (154) galaxies with spectra showing strong emission lines and with $R < 22.8$ is shown for the redshift range $0.25 < z < 1.05$. The solid line indicates the ranking of the ISO galaxies within the sample using $L(B)$, the dashed line is for $L(R)$, and the dot-dashed line utilizes the mid-IR luminosity predicted using the formalism of Meurer *et al.* (1999).

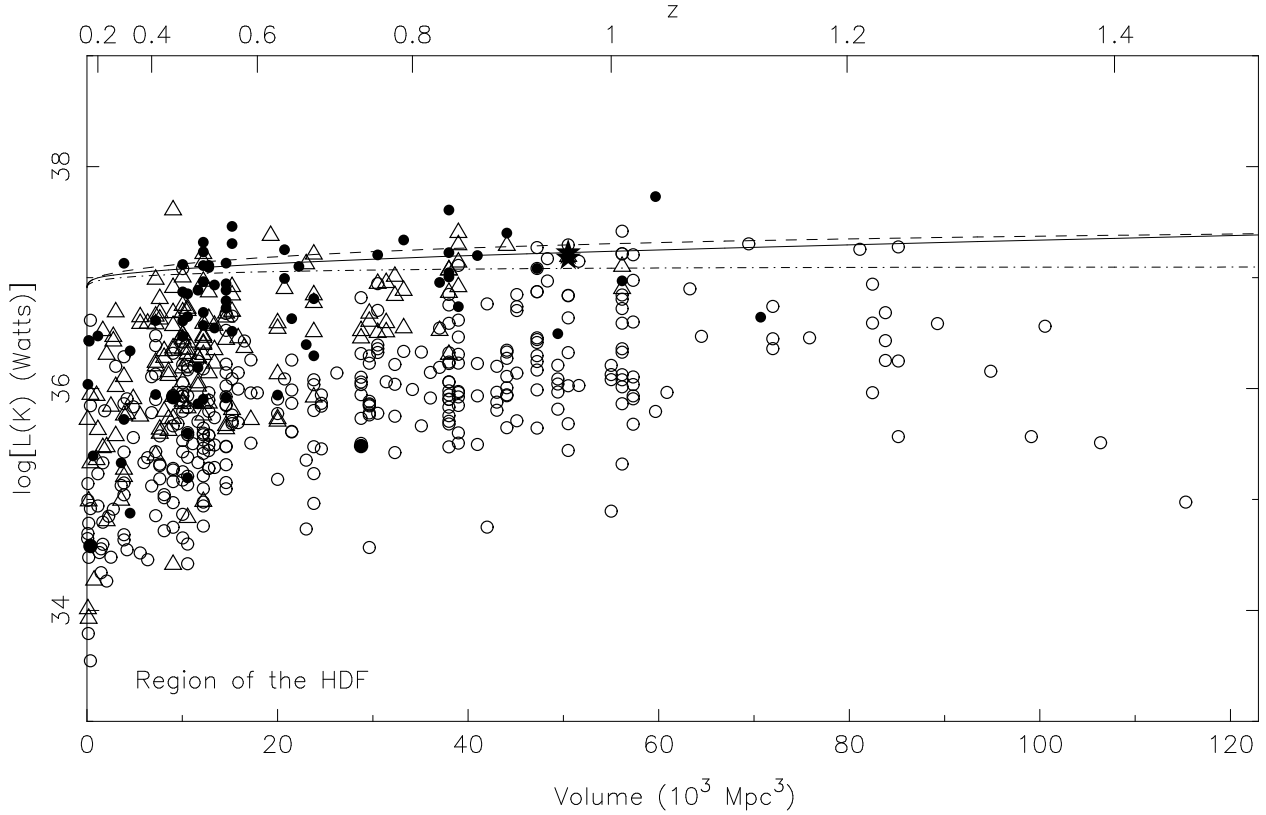


Fig. 11.— $L(K)$ is shown as a function of the cosmological comoving volume for galaxies in the region of the HDF with secure redshifts. The plot symbols are the same as in Figure 7. The lines at the top of the distribution represent the track of a galaxy of a L^* (at K) galaxy with $L = 10^{11}L_{\odot}$ (at $z = 0$) of type E, Sa and Sc with evolutionary corrections at K calculated by Poggianti (1997) applied for $z > 0$.

Table 1. SED Parameters for Objects in the Region of the HDF

RA (–12h)	Dec ^a (–62°)	log[L(B)] (W) ^b	α_{UV} (2p)	α_{IR} (2p)	α_{UV} (sBB)	log(L(λ_m :blue)) (W)	T (sBB)	log(L(λ_m :red)) (W)
36 15.90	12 37.3	36.90	2.61	0.65	1.32	36.69	5712	36.66
36 17.60	14 2.2	36.93	0.91	0.68	0.71	36.92	7311	36.95
36 17.69	13 44.3	36.84	6.01	1.65	7.12	36.77	4662	36.74
36 17.65	14 8.1	36.71	1.40	1.53	1.07	36.64	5631	36.79
36 18.70	11 54.1	36.63	2.43	1.73	2.54	36.62	5134	36.73
36 19.41	14 28.7	36.61	1.93	1.10	1.71	36.54	5981	36.64
36 19.50	11 58.9	36.78	1.16	0.69	0.90	36.73	6941	36.79
36 19.47	12 52.5	37.05	4.45	1.40	3.64	36.80	4720	36.92
36 19.72	13 53.1	36.45	5.72	1.19	4.55	36.11	4398	36.14
36 19.89	13 47.8	36.86	2.13	0.89	1.75	36.77	5974	36.88
36 21.03	12 3.8	36.71	2.74	1.08	2.12	36.57	5337	36.67
36 21.12	12 7.9	36.99	2.85	1.62	2.78	36.96	5630	37.05
36 21.20	13 6.4	36.25	3.47	1.00	2.78	36.07	5402	36.18
36 21.27	11 0.5	36.16	1.87	0.55	1.01	35.97	6515	36.15
36 21.33	11 10.7	17.40	7.27	0.71	5.53	36.99	5316	36.99
36 21.33	14 17.1	36.78	4.23	1.74	4.34	36.70	4344	36.75
36 21.57	12 26.8	36.82	3.45	0.97	2.21	36.61	5444	36.73
36 21.59	13 0.3	37.00	2.59	1.21	2.16	36.90	5454	36.99
36 21.59	11 22.4	36.13	1.23	0.38	0.17	35.90	6170	36.14
36 21.73	13 13.5	35.70	1.96	0.65	1.68	35.63	5690	35.60
36 22.21	12 37.2	36.53	2.83	1.52	1.47	36.24	4975	36.50
36 22.22	11 6.2	36.16	2.73	0.68	2.21	36.04	5592	36.03
36 22.34	12 41.3	36.73	3.28	1.09	2.30	36.51	4980	36.64
36 22.82	12 59.7	36.94	6.03	1.23	4.40	36.62	4847	36.77
36 23.06	13 46.3	36.70	2.49	1.52	2.35	36.66	5062	36.72
36 22.98	14 31.0	35.59	3.13	0.70	2.61	35.54	5554	35.53
36 24.02	11 9.6	36.56	2.13	1.09	2.04	36.55	5695	36.58
36 24.16	15 14.4	35.05	2.03	0.11	1.98	35.01	6623	35.03
36 24.41	14 54.1	37.19	6.16	1.92	5.86	37.06	4610	37.17
36 24.31	15 25.3	36.48	4.77	1.37	4.05	36.20	4683	36.33
36 24.55	11 11.2	36.81	3.69	1.54	3.53	36.70	4965	36.77
36 24.54	11 39.3	35.93	1.81	0.29	1.78	35.94	6990	35.89
36 24.44	14 48.0	36.28	3.81	1.57	3.81	36.20	4650	36.23
36 24.68	14 18.7	36.60	0.24	–0.09	–0.03	36.50	31660	36.50

Table 1—Continued

RA (−12h)	Dec ^a (−62°)	log[L(B)] (W) ^b	α_{UV} (2p)	α_{IR} (2p)	α_{UV} (sBB)	log(L(λ_m :blue) (W)	T (sBB)	log(L(λ_m :red) (W)
36 24.71	15 10.4	37.10	3.39	1.81	2.96	36.97	4982	37.21
36 24.91	14 38.7	36.81	5.33	1.69	4.98	36.55	4461	36.70
36 24.95	12 52.1	36.22	2.85	0.89	2.21	36.04	5768	36.19
36 25.08	13 0.5	36.76	4.76	1.60	3.85	36.42	4584	36.74
36 25.07	13 41.8	35.73	1.10	1.43	0.58	35.69	5482	35.76
36 25.20	14 10.7	35.24	2.56	1.06	1.78	35.09	5369	35.24
36 25.36	12 35.2	35.96	3.37	1.43	2.26	35.66	4886	35.86
36 25.45	15 19.6	36.59	1.31	0.84	1.05	36.52	6910	36.63
36 25.99	14 11.4	35.74	2.04	0.84	0.97	35.56	5330	35.68
36 26.63	12 52.0	36.88	2.15	0.89	1.18	36.74	5761	36.89
36 26.66	10 19.4	35.39	1.62	−0.63	1.11	35.33	11185	35.33
36 27.07	15 9.4	37.36	6.84	1.34	6.96	37.10	4708	37.17
36 27.10	10 2.0	36.90	1.11	0.57	1.28	37.00	8130	37.08
36 27.31	12 57.9	37.18	1.46	1.28	1.58	37.25	5993	37.25
36 27.46	10 17.6	36.30	2.11	−0.20	1.37	36.18	7604	36.14
36 27.55	14 18.8	36.54	1.33	0.31	1.38	36.60	8498	36.58
36 27.53	15 41.2	36.15	2.09	1.03	2.03	36.10	5858	36.21
36 27.88	11 24.1	36.52	2.15	1.05	1.24	36.37	5240	36.46
36 27.82	12 40.6	36.57	5.48	1.37	5.72	36.46	5012	36.54
36 27.89	14 49.0	36.87	5.30	1.96	4.49	36.64	4202	36.77
36 28.04	15 7.4	36.11	1.93	1.41	2.35	36.20	5397	36.24
36 28.26	12 37.5	36.54	2.52	0.98	1.54	36.33	5643	36.51
36 28.24	14 32.8	35.92	2.92	0.95	2.57	35.84	5127	35.82
36 28.43	10 37.0	36.39	1.30	0.57	1.19	36.38	7359	36.40
36 28.53	9 51.4	36.65	1.03	0.75	0.96	36.67	6956	36.67
36 28.72	10 23.3	36.91	1.21	1.24	0.94	36.86	5586	36.92
36 28.73	13 57.8	36.10	2.62	0.85	1.40	35.80	6058	36.06
36 28.80	12 39.3	36.06	0.15	0.35	−0.07	36.04	17615	36.09
36 29.01	13 46.6	36.25	1.70	0.71	1.40	36.20	6381	36.26
36 29.13	11 53.0	36.06	1.23	0.53	0.57	35.98	6567	36.04
36 29.07	13 52.1	37.03	1.63	−1.11	1.67	37.00	26604	37.00
36 29.14	10 46.0	36.86	4.02	2.30	3.81	36.72	4120	36.72
36 29.68	14 20.6	37.24	3.00	−0.73	2.97	37.18	13320	37.18
36 29.70	13 25.0	36.23	0.81	0.89	0.58	36.21	6278	36.24

Table 1—Continued

RA (−12h)	Dec ^a (−62°)	log[L(B)] (W) ^b	α_{UV} (2p)	α_{IR} (2p)	α_{UV} (sBB)	log(L(λ_m :blue) (W)	T (sBB)	log(L(λ_m :red) (W)
36 29.77	13 29.7	36.44	1.38	0.93	1.17	36.43	6284	36.45
36 29.98	14 3.1	36.91	2.40	1.30	1.97	36.77	5089	36.89
36 30.03	12 24.2	35.66	0.41	0.95	0.21	35.72	6161	35.76
36 29.91	14 40.9	36.57	2.76	1.27	2.43	36.44	5122	36.52
36 30.24	10 14.0	36.10	1.86	0.60	1.26	35.99	6841	36.11
36 30.42	12 8.5	36.44	1.14	1.26	1.21	36.52	5920	36.64
36 30.38	15 58.6	35.49	3.09	0.16	2.03	35.31	6956	35.34
36 30.62	15 33.7	36.28	1.91	0.62	0.89	36.09	6606	36.27
36 30.77	10 58.7	36.34	3.19	0.72	2.08	36.15	5500	36.17
36 30.87	14 33.4	36.32	2.44	1.21	2.08	36.24	5306	36.37
36 31.20	12 36.3	36.30	1.16	0.94	1.13	36.30	6573	36.40
36 31.47	11 13.9	37.07	1.63	1.20	1.50	37.06	5795	37.06
36 31.62	16 4.0	37.14	2.70	0.92	2.42	37.04	5807	37.10
36 31.90	12 40.4	36.50	1.72	0.43	0.94	36.38	7287	36.51
36 32.01	10 20.4	35.58	1.63	0.42	1.13	35.53	6998	35.55
36 32.02	12 24.8	35.11	1.12	0.38	0.77	35.06	7171	35.05
36 32.43	10 37.6	35.91	2.81	0.21	1.88	35.75	6404	35.75
36 32.47	11 5.1	37.25	7.18	1.42	5.76	37.02	4524	37.06
36 32.55	11 13.3	36.07	5.35	1.10	3.95	35.79	5303	35.99
36 32.47	15 13.2	36.67	3.20	1.52	2.27	36.42	4793	36.65
36 32.71	12 39.2	35.68	0.96	0.12	0.76	35.72	7702	35.85
36 32.77	12 43.8	36.56	3.96	1.76	3.34	36.36	4412	36.52
36 33.17	11 34.0	35.11	1.78	0.45	1.93	35.37	6888	35.23
36 33.16	15 13.8	36.33	2.43	0.97	1.69	36.19	5418	36.27
36 33.21	12 35.6	36.66	0.78	1.18	0.65	36.71	6106	36.71
36 33.25	14 11.0	36.69	0.51	−0.38	0.39	36.67	11821	36.67
36 33.62	10 5.6	37.12	1.88	1.78	1.81	37.08	4763	37.08
36 33.60	13 19.8	37.08	2.48	1.49	2.00	36.93	5058	37.06
36 33.76	11 56.4	36.03	1.17	1.11	1.26	36.14	5960	36.23
36 33.70	14 31.0	36.67	4.76	1.89	4.98	36.61	4121	36.65
36 34.06	10 45.8	36.56	1.09	1.12	1.03	36.57	5652	36.57
36 34.00	10 54.4	36.87	1.30	0.68	1.26	36.89	6966	36.94
36 33.99	16 4.6	36.65	1.43	0.77	1.12	36.60	6550	36.65
36 34.17	13 5.8	36.13	2.34	1.87	2.07	35.99	4792	36.10

Table 1—Continued

RA (−12h)	Dec ^a (−62°)	log[L(B)] (W) ^b	α_{UV} (2p)	α_{IR} (2p)	α_{UV} (sBB)	log(L(λ_m :blue)) (W)	T (sBB)	log(L(λ_m :red)) (W)
36 34.28	14 33.0	36.88	5.90	1.76	5.00	36.67	4621	36.88
36 34.26	14 48.3	35.97	0.95	0.20	0.56	35.95	7928	36.06
36 34.36	13 12.5	36.52	2.01	1.06	1.47	36.36	5649	36.52
36 34.46	12 13.2	37.45	4.44	1.46	3.28	37.21	4304	37.23
36 34.56	12 40.9	37.02	1.73	2.18	1.46	36.96	4446	36.96
36 34.50	14 29.7	36.07	2.56	0.44	1.99	35.96	6782	36.09
36 34.97	12 24.1	37.36	4.09	1.50	2.97	37.12	4553	37.22
36 34.84	16 28.3	36.71	1.50	0.72	0.80	36.62	7058	36.63
36 34.91	15 48.6	35.46	1.69	2.11	1.48	35.39	4236	35.49
36 35.30	11 9.7	36.56	5.53	1.27	4.86	36.26	4588	36.39
36 36.28	13 19.8	36.44	0.99	0.47	0.59	36.37	7703	36.49
36 36.35	12 28.2	36.30	2.37	1.42	2.20	36.25	5277	36.39
36 36.29	15 0.7	35.97	1.24	0.42	0.19	35.78	6582	35.95
36 36.50	13 40.7	36.59	5.33	1.85	4.11	36.25	4075	36.42
36 36.40	12 37.3	36.81	2.39	1.63	2.11	36.73	4820	36.73
36 36.59	15 24.5	36.40	0.14	0.20	0.14	36.32	9546	36.41
36 36.65	13 46.6	37.53	0.91	0.78	1.13	37.66	6665	37.66
36 36.76	11 56.0	36.42	2.79	1.33	1.89	36.23	5012	36.41
36 36.79	12 13.1	37.44	3.02	1.64	2.80	37.33	4497	37.34
36 36.86	11 34.8	36.18	2.07	0.45	1.47	36.25	6538	36.18
36 37.04	11 59.5	36.84	1.58	1.01	1.44	36.90	6051	36.92
36 37.36	12 52.3	36.42	4.47	1.66	5.05	36.39	4741	36.50
36 37.62	12 40.7	36.61	1.31	0.85	1.54	36.71	6450	36.75
36 37.80	11 49.4	36.62	2.41	1.98	2.12	36.54	4367	36.61
36 37.97	9 22.0	37.08	2.92	1.38	2.86	37.00	5321	37.04
36 37.97	16 15.2	36.66	5.82	1.11	6.04	36.49	5122	36.56
36 38.03	9 27.7	35.88	2.91	0.79	2.17	35.69	5690	35.76
36 38.40	9 53.3	36.90	3.01	0.51	1.10	36.55	6851	36.70
36 38.13	11 16.2	36.95	1.08	1.10	1.36	37.06	6083	37.06
36 38.29	11 50.8	36.75	3.39	1.60	2.93	36.55	4902	36.68
36 38.20	16 4.9	37.32	7.30	1.31	7.14	37.00	4605	37.08
36 38.48	13 12.9	36.38	1.17	0.46	0.33	36.23	6784	36.42
36 38.63	13 38.9	35.60	1.57	2.06	1.11	35.58	4535	35.65
36 38.80	15 58.6	35.98	3.25	1.12	1.93	35.71	4753	35.79

Table 1—Continued

RA (−12h)	Dec ^a (−62°)	log[L(B)] (W) ^b	α_{UV} (2p)	α_{IR} (2p)	α_{UV} (sBB)	log(L(λ_m :blue) (W)	T (sBB)	log(L(λ_m :red) (W)
36 38.67	15 10.1	35.52	1.31	1.94	1.37	35.62	5133	35.70
36 38.76	15 47.1	36.95	1.66	0.25	1.04	36.79	7592	36.94
36 38.90	11 18.6	36.62	0.32	0.84	0.06	36.63	6702	36.66
36 38.86	11 28.6	35.38	0.94	0.97	1.52	35.54	6985	35.53
36 38.87	12 57.1	37.22	1.95	1.75	1.88	37.19	4809	37.19
36 38.93	9 11.5	35.77	2.44	−0.48	2.33	35.73	8711	35.71
36 39.00	12 45.0	35.95	3.07	1.23	2.86	35.84	5375	35.94
36 39.06	10 6.1	36.81	1.85	0.98	1.26	36.69	5694	36.82
36 39.28	15 52.1	35.82	2.70	0.75	2.30	35.71	5929	35.79
36 39.22	16 23.4	37.09	5.89	1.10	4.33	36.51	5173	36.78
36 39.70	15 26.2	36.54	2.56	1.60	2.40	36.49	4840	36.54
36 39.68	10 9.7	36.36	3.20	1.34	3.33	36.30	5361	36.39
36 39.75	15 47.7	37.36	7.09	1.12	7.09	37.08	4873	37.14
36 39.83	10 1.7	35.16	2.18	0.27	0.57	35.03	6522	35.03
36 39.92	12 50.0	37.17	2.78	1.26	2.44	37.06	5254	37.14
36 39.95	10 29.2	37.02	3.63	1.37	3.02	36.80	5275	36.95
36 40.12	13 5.5	36.64	4.77	1.75	5.45	36.59	4727	36.70
36 40.32	13 31.0	35.95	4.07	1.98	3.65	35.75	4166	35.89
36 40.50	10 3.3	36.58	2.44	1.36	2.47	36.54	5164	36.56
36 40.49	13 22.9	35.54	2.29	0.16	2.36	35.51	7783	35.54
36 40.88	10 54.7	36.69	1.30	0.77	1.01	36.63	6637	36.71
36 41.30	9 48.8	36.73	3.43	1.05	2.18	36.49	4927	36.52
36 41.17	14 21.0	36.54	2.78	1.08	2.26	36.40	5302	36.50
36 41.13	13 14.3	36.74	1.49	1.34	1.49	36.72	5421	36.72
36 41.33	15 47.6	35.83	2.25	0.91	2.25	35.77	5672	35.83
36 41.37	9 48.1	37.02	6.01	1.67	4.79	36.79	4266	36.83
36 41.47	14 2.7	36.94	5.58	1.22	5.61	36.70	4842	36.78
36 41.53	9 2.9	36.59	1.25	0.57	1.23	36.57	6181	36.51
36 41.68	13 24.2	35.84	1.73	0.77	0.96	35.68	5835	35.87
36 41.74	9 43.3	37.00	5.07	1.49	5.41	36.84	4685	36.83
36 42.04	13 21.2	36.15	1.06	1.19	0.65	36.05	5786	36.16
36 42.16	15 45.2	37.27	3.71	1.67	3.75	37.13	4519	37.14
36 42.41	12 52.2	36.77	1.16	1.39	1.20	36.77	6067	36.77
36 42.53	9 33.8	36.91	3.66	1.21	3.25	36.70	4890	36.79

Table 1—Continued

RA (−12h)	Dec ^a (−62°)	log[L(<i>B</i>)] (W) ^b	α_{UV} (2p)	α_{IR} (2p)	α_{UV} (sBB)	log(L(λ_m :blue) (W)	<i>T</i> (sBB)	log(L(λ_m :red) (W)
36 42.55	11 21.9	36.46	1.05	0.87	0.69	36.39	6381	36.48
36 42.55	15 18.4	36.41	1.79	0.47	0.74	36.20	7551	36.40
36 42.71	13 6.7	36.10	3.04	1.82	2.84	35.97	4413	36.10
36 42.73	15 2.7	36.18	1.79	1.11	1.72	36.14	5748	36.18
36 43.01	10 30.2	36.49	2.24	0.67	1.00	36.28	6310	36.42
36 43.12	11 8.5	35.56	2.78	1.18	2.83	35.48	4654	35.38
36 43.03	16 31.9	36.70	1.19	0.23	1.06	36.66	8746	36.77
36 43.50	15 32.2	36.60	1.72	0.56	1.56	36.52	7567	36.61
36 43.20	16 24.9	35.40	1.44	1.20	−0.73	35.15	4544	35.15
36 43.75	13 56.7	35.99	2.78	0.55	2.31	35.89	5648	35.84
36 44.27	15 18.2	36.21	1.79	0.24	0.81	35.99	6663	36.18
36 44.48	10 17.9	35.96	2.70	0.98	2.41	35.83	5440	35.90
36 44.38	10 36.7	36.64	1.14	0.30	0.82	36.56	8276	36.65
36 44.61	9 26.6	36.53	2.53	1.26	1.80	36.34	4901	36.39
36 44.61	13 4.6	36.57	3.88	1.59	3.41	36.36	4565	36.46
36 44.80	14 55.2	36.50	1.48	0.42	1.40	36.46	8149	36.59
36 44.94	16 16.6	36.81	1.47	0.74	1.18	36.72	6025	36.78
36 45.80	13 25.8	36.31	2.10	0.69	1.82	36.20	6929	36.27
36 45.42	15 23.0	36.57	0.87	0.54	0.19	36.43	6708	36.57
36 45.86	13 25.7	36.23	1.81	0.98	1.82	36.19	5433	36.24
36 45.97	11 1.2	37.09	5.07	1.40	4.38	36.76	4741	36.93
36 46.22	15 27.3	36.94	2.30	1.65	1.88	36.78	4569	36.88
36 46.31	16 14.5	36.47	2.91	0.92	1.96	36.21	5323	36.34
36 46.32	16 29.2	37.01	7.88	1.15	7.09	36.91	4970	36.84
36 46.84	10 20.1	34.97	2.61	0.36	2.50	34.88	7228	34.88
36 46.86	14 47.1	36.82	4.07	1.29	3.56	36.63	4976	36.75
36 46.84	15 40.6	36.99	2.26	1.03	1.98	36.86	5921	37.00
36 46.94	9 6.6	36.38	2.17	1.49	1.53	36.17	5172	36.37
36 47.38	16 20.3	36.43	2.98	0.70	2.21	36.21	5894	36.34
36 47.28	16 28.3	37.46	5.20	0.86	4.78	37.15	5107	37.21
36 47.76	15 12.7	36.57	2.19	0.66	1.23	36.36	5878	36.51
36 47.80	10 45.6	37.14	2.57	1.15	2.33	36.94	5864	36.94
36 48.12	11 2.2	36.40	2.78	1.14	2.33	36.22	5236	36.32
36 48.18	10 2.5	36.60	1.27	0.54	1.17	36.58	7303	36.65

Table 1—Continued

RA (−12h)	Dec ^a (−62°)	log[L(B)] (W) ^b	α_{UV} (2p)	α_{IR} (2p)	α_{UV} (sBB)	log(L(λ_m :blue) (W)	T (sBB)	log(L(λ_m :red) (W)
36 48.15	15 24.9	35.94	1.15	0.15	0.64	35.85	7519	35.94
36 48.28	15 7.4	37.20	3.43	0.49	2.59	36.86	6970	36.85
36 48.48	15 40.4	36.06	1.32	0.79	1.36	36.05	6432	36.13
36 48.58	9 32.1	36.71	2.48	0.93	1.70	36.50	5086	36.59
36 48.61	11 41.1	37.47	5.82	1.12	5.74	37.24	4955	37.24
36 48.60	15 52.4	35.67	4.01	2.31	2.35	35.30	3798	35.62
36 49.03	15 12.1	35.89	1.89	0.87	1.74	35.81	5588	35.85
36 49.04	16 20.6	37.90	4.71	1.00	4.71	37.72	8990	37.72
36 49.46	14 56.5	35.01	0.16	0.96	−0.16	35.02	5987	34.99
36 49.62	11 12.8	36.32	1.03	0.62	0.94	36.33	6879	36.41
36 49.65	15 34.2	35.35	3.04	0.39	3.23	35.27	6582	35.27
36 49.94	9 35.4	35.63	4.41	0.07	3.32	35.36	7018	35.47
36 49.93	10 58.6	36.36	1.75	0.82	1.32	36.22	6448	36.36
36 49.95	16 37.1	36.61	2.82	0.69	1.64	36.32	5567	36.46
36 50.27	11 27.4	36.62	0.87	0.57	0.85	36.64	7007	36.64
36 50.23	16 16.2	36.16	6.06	0.82	5.53	35.87	5423	35.99
36 50.71	10 58.8	36.60	1.98	0.39	0.88	36.41	6697	36.54
36 51.07	9 38.6	35.84	2.24	0.14	1.64	35.72	6431	35.66
36 51.09	10 30.9	36.83	5.15	1.61	3.40	36.54	4297	36.60
36 51.61	9 54.5	35.48	2.90	0.19	2.20	35.33	6349	35.33
36 51.64	10 52.3	35.90	0.83	−0.13	−0.22	35.74	8422	35.89
36 51.84	11 25.4	37.06	1.44	−0.76	1.40	37.15	18758	37.08
36 52.11	14 57.0	36.03	1.58	0.62	1.36	36.03	6624	36.04
36 52.29	9 31.8	35.40	2.58	−0.10	2.64	35.33	7934	35.32
36 52.37	10 19.9	36.11	2.13	0.50	0.78	35.84	5829	35.99
36 52.30	15 37.0	37.26	6.13	1.13	6.03	36.96	4907	37.01
36 52.49	9 19.6	37.31	6.60	0.77	6.60	37.03	5291	37.03
36 52.43	16 37.8	36.00	1.51	0.52	0.45	35.79	6033	35.92
36 52.44	10 35.7	36.08	1.58	0.16	0.82	35.95	6829	35.95
36 52.86	14 43.9	36.95	6.96	1.41	5.48	36.73	4413	36.81
36 52.87	14 53.7	34.75	2.58	0.07	2.31	34.66	7259	34.62
36 52.99	15 8.6	37.15	5.33	1.20	4.69	36.79	5010	36.94
36 52.93	16 42.0	35.61	1.98	0.85	1.71	35.51	5791	35.57
36 53.20	11 16.9	37.15	2.50	1.65	1.87	36.90	4914	37.10

Table 1—Continued

RA (−12h)	Dec ^a (−62°)	log[L(<i>B</i>)] (W) ^b	α_{UV} (2p)	α_{IR} (2p)	α_{UV} (sBB)	log(L(λ_m :blue) (W)	<i>T</i> (sBB)	log(L(λ_m :red) (W)
36 53.43	11 40.3	36.93	0.69	1.50	0.32	36.78	5608	36.78
36 53.90	16 6.9	36.57	1.15	0.42	0.87	36.50	7513	36.63
36 54.02	10 46.3	36.22	1.27	0.12	-0.29	35.95	7352	36.13
36 54.13	15 14.9	36.51	0.59	−0.23	0.38	36.48	12240	36.61
36 54.36	14 34.2	36.38	1.51	0.68	0.49	36.16	6094	36.34
36 54.57	10 14.6	34.85	2.53	0.56	1.78	34.70	6161	34.70
36 54.61	11 27.2	36.01	3.06	1.56	3.52	35.98	4194	35.86
36 54.83	15 57.2	37.41	4.29	1.00	4.29	37.25	7247	37.25
36 55.28	9 12.6	35.99	3.03	0.56	1.92	35.73	5666	35.81
36 55.57	11 35.6	36.26	1.32	0.59	0.44	36.07	6135	36.21
36 55.70	9 17.4	36.62	4.67	1.46	3.77	36.29	4192	36.36
36 55.80	9 25.4	36.22	2.49	0.24	1.73	36.05	6550	36.09
36 55.91	11 40.8	35.66	2.00	0.66	1.96	35.18	5208	35.38
36 55.98	14 54.5	35.90	3.69	0.96	3.95	35.80	5508	35.88
36 56.39	12 9.3	35.34	1.48	0.19	1.35	35.30	7556	35.34
36 56.49	14 19.7	35.43	2.50	0.18	2.25	35.34	6848	35.31
36 57.49	12 11.0	36.98	3.45	1.58	2.84	36.75	4690	36.93
36 57.57	14 37.7	35.43	1.84	0.35	1.96	35.40	7082	35.42
36 57.76	14 54.8	36.96	3.79	1.37	3.08	36.68	5094	36.87
36 57.85	10 12.8	36.13	6.00	0.92	7.04	35.95	5201	36.00
36 58.06	11 37.8	36.17	0.60	−0.09	0.18	36.10	9902	36.19
36 58.26	9 23.1	36.37	2.58	0.47	2.03	36.18	6420	36.30
36 58.30	9 58.1	36.86	3.79	0.79	2.47	36.60	5030	36.60
36 58.35	12 14.1	36.40	0.46	0.56	0.62	36.50	8647	36.50
36 58.36	15 48.6	36.49	0.33	0.60	0.33	36.51	7636	36.60
36 58.82	14 34.8	37.14	3.04	1.46	2.67	36.95	5011	37.09
36 58.76	16 37.8	36.88	3.74	0.77	2.39	36.59	4856	36.59
36 58.96	12 8.8	37.00	3.48	1.85	2.92	36.75	4585	36.91
36 59.44	14 4.5	35.77	2.85	0.14	1.93	35.60	6948	35.54
36 59.54	11 53.9	36.88	1.07	1.21	0.87	36.83	5732	36.83
36 59.89	14 49.8	37.04	2.85	1.38	2.65	36.89	5116	36.96
37 0.04	16 5.7	36.90	1.03	0.75	1.31	36.98	7492	36.98
37 0.36	16 16.9	36.94	1.92	1.14	1.52	36.78	5485	36.89
37 0.51	14 5.8	36.46	2.85	1.65	3.19	36.43	4846	36.52

Table 1—Continued

RA (−12h)	Dec ^a (−62°)	log[L(B)] (W) ^b	α_{UV} (2p)	α_{IR} (2p)	α_{UV} (sBB)	log(L(λ_m :blue)) (W)	T (sBB)	log(L(λ_m :red)) (W)	
37	0.73	11 7.3	36.41	1.07	0.69	0.90	36.36	6534	36.45
37	1.07	13 19.7	35.51	3.70	2.47	5.14	35.46	4108	35.63
37	1.44	11 35.7	36.48	2.29	0.90	1.60	36.28	5467	36.41
37	1.51	11 29.0	37.07	2.31	1.43	2.17	36.97	5336	37.05
37	1.77	11 44.0	36.71	1.68	0.00	2.06	36.76	9906	36.69
37	1.57	11 46.6	35.90	1.30	3.56	−0.08	35.67	3584	35.87
37	1.92	15 10.3	36.90	1.05	0.92	0.82	36.83	6977	36.99
37	1.87	16 21.8	35.77	5.28	0.52	3.13	35.15	5250	35.44
37	1.93	9 39.0	36.57	1.45	0.38	1.23	36.49	7547	36.54
37	1.91	10 24.6	36.65	3.87	1.18	3.05	36.40	4675	36.47
37	2.00	11 22.9	36.41	2.58	0.54	2.31	36.29	5772	36.19
37	2.00	13 23.0	36.39	1.64	1.52	1.75	36.36	5379	36.50
37	2.03	13 48.8	36.08	0.87	0.18	0.27	35.98	7968	36.15
37	2.07	15 17.3	36.24	2.33	1.08	1.86	36.08	5722	36.18
37	2.24	12 43.2	34.68	2.42	0.28	3.30	34.65	7543	34.59
37	2.49	13 42.0	36.67	1.20	0.68	0.81	36.57	6524	36.67
37	2.67	13 47.2	35.89	1.27	0.53	0.29	35.71	6133	35.81
37	2.73	14 1.7	37.33	2.55	1.52	2.52	37.24	4983	37.24
37	2.54	14 48.4	36.23	2.91	0.99	1.91	35.96	5747	36.16
37	2.60	12 16.6	36.65	2.63	2.23	2.46	36.57	4398	36.57
37	2.81	11 10.4	36.56	3.24	1.62	2.77	36.36	4630	36.49
37	2.89	14 23.7	36.84	2.94	1.85	2.85	36.78	4961	36.92
37	2.92	14 27.6	36.35	1.88	0.72	1.69	36.26	7158	36.39
37	2.71	15 43.5	37.21	1.07	1.49	1.01	37.18	5231	37.28
37	2.77	16 36.7	35.74	2.07	−0.95	1.00	35.55	11986	35.64
37	3.27	14 17.8	36.73	4.77	1.26	5.19	36.61	5036	36.67
37	3.34	16 31.8	36.11	3.89	1.13	2.27	35.75	4914	35.77
37	3.52	10 48.4	36.06	2.55	0.50	1.82	35.90	6387	35.99
37	3.50	11 2.0	36.54	4.65	1.22	4.04	36.34	5034	36.46
37	3.80	13 53.1	36.78	0.60	0.58	0.62	36.83	6744	36.82
37	3.87	10 9.4	35.98	0.88	−0.11	0.29	35.91	7732	35.90
37	3.90	14 41.1	36.32	1.22	0.82	1.08	36.31	6507	36.42
37	4.00	15 23.2	35.99	2.20	0.91	2.20	35.93	5666	35.97
37	4.24	16 24.8	36.51	3.08	0.99	2.62	36.35	5005	36.39

Table 1—Continued

RA (−12h)	Dec ^a (−62°)	log[L(B)] (W) ^b	α_{UV} (2p)	α_{IR} (2p)	α_{UV} (sBB)	log(L(λ_m :blue)) (W)	T (sBB)	log(L(λ_m :red)) (W)	
37	4.20	12 39.6	36.43	1.02	1.02	0.99	36.43	6427	36.42
37	4.50	10 3.8	36.02	1.90	0.19	1.35	35.91	6190	35.83
37	4.61	14 16.0	36.37	0.69	0.78	0.69	36.39	7185	36.39
37	4.64	10 28.6	36.19	2.66	0.91	2.14	36.13	5756	36.14
37	4.62	14 29.1	36.83	3.58	1.45	2.92	36.62	4718	36.76
37	5.15	12 10.8	35.80	1.29	0.60	1.15	35.75	6609	35.81
37	5.02	15 46.9	36.04	2.14	0.35	1.32	35.84	6780	36.00
37	5.57	11 29.2	36.94	1.72	0.08	1.69	36.90	8304	36.90
37	5.70	13 3.3	35.05	3.48	0.18	2.96	34.91	6341	34.89
37	5.75	15 25.1	36.25	1.75	0.89	1.56	36.18	5924	36.31
37	5.84	11 53.8	37.39	2.38	1.39	2.00	37.24	5377	37.40
37	5.81	13 17.2	36.74	1.48	0.53	1.24	36.71	6631	36.71
37	5.83	14 23.4	37.10	2.71	1.65	2.63	37.01	4762	37.01
37	6.19	13 32.7	36.83	2.07	1.04	1.67	36.72	5498	36.76
37	6.27	15 17.7	36.77	0.59	0.23	0.29	36.75	10812	36.94
37	6.41	15 21.5	36.03	1.75	1.09	1.46	35.96	5731	36.10
37	6.54	15 12.5	36.48	1.20	0.18	0.87	36.40	8438	36.48
37	6.89	9 59.8	36.37	2.62	0.30	1.43	36.13	6464	36.23
37	6.93	12 8.0	35.78	0.62	0.94	0.58	35.79	6215	35.83
37	7.23	11 57.8	36.26	1.31	0.49	0.39	36.06	6817	36.24
37	7.25	12 14.1	36.62	5.03	1.42	4.87	36.37	4866	36.54
37	7.42	13 56.7	36.19	1.52	1.04	1.07	36.06	6046	36.18
37	7.62	11 12.1	36.77	4.47	0.97	4.81	36.66	5251	36.68
37	7.75	11 37.7	36.22	1.08	0.04	0.37	36.07	8022	36.21
37	7.87	16 2.0	36.01	1.40	0.55	0.30	35.81	6034	35.97
37	7.84	16 5.7	37.27	2.73	1.46	2.03	37.01	4914	37.20
37	8.00	14 44.5	36.29	3.29	1.14	2.96	36.13	5358	36.25
37	8.08	12 46.8	36.64	1.48	0.28	0.71	36.44	7407	36.62
37	8.16	12 15.3	36.42	1.66	0.66	1.02	36.25	6491	36.40
37	8.31	12 52.5	36.85	1.79	0.88	1.29	36.72	6033	36.85
37	8.33	13 20.8	36.44	1.05	0.34	0.80	36.39	7850	36.46
37	8.12	14 22.6	37.27	5.30	1.52	3.88	36.96	4728	37.15
37	8.29	10 56.1	36.95	2.39	0.91	1.61	36.85	5468	36.83
37	8.34	14 53.9	36.44	1.39	0.20	0.62	36.27	7775	36.46

Table 1—Continued

RA (–12h)	Dec ^a (–62°)	log[L(B)] (W) ^b	α_{UV} (2p)	α_{IR} (2p)	α_{UV} (sBB)	log(L(λ_m :blue) (W)	T (sBB)	log(L(λ_m :red) (W)	
37	8.36	15 14.6	37.10	1.62	0.50	1.22	36.96	6864	37.07
37	8.62	10 51.2	36.60	2.75	1.10	1.63	36.46	5161	36.51
37	8.66	11 28.5	36.76	0.27	0.20	0.22	36.76	8946	36.79
37	8.65	15 1.4	36.60	4.96	1.11	4.75	36.37	5181	36.50
37	8.88	11 17.9	36.18	2.97	1.27	2.26	35.93	5000	36.10
37	8.95	12 2.2	36.52	1.04	0.55	0.52	36.41	7247	36.53
37	8.83	12 14.4	36.05	1.18	0.40	0.88	35.96	7521	36.08
37	9.20	12 10.9	35.70	1.35	0.25	0.72	35.56	6912	35.71
37	9.50	14 49.1	35.72	1.93	0.55	1.89	35.64	6122	35.67
37	9.56	14 23.4	36.66	5.96	1.07	5.75	36.39	5184	36.51
37	9.61	10 55.2	36.40	0.95	0.04	0.73	36.36	9391	36.42
37	9.85	15 23.9	36.56	5.34	0.94	4.53	36.29	4712	36.31
37	10.36	13 19.7	35.87	3.04	0.50	2.79	35.73	7060	35.84
37	10.24	10 58.9	36.09	2.46	0.43	1.74	35.90	6755	36.04
37	10.56	11 41.0	37.10	1.84	1.34	1.73	37.06	5348	37.11
37	10.58	13 41.6	36.61	1.86	0.68	1.63	36.50	6645	36.58
37	10.91	10 59.0	36.05	1.97	0.44	1.32	35.89	6772	36.02
37	10.86	11 29.1	35.75	1.46	0.43	1.54	35.76	7417	35.89
37	11.08	10 47.6	35.77	2.04	0.44	2.23	35.44	5773	35.46
37	11.36	15 45.1	36.42	1.00	0.41	0.00	36.23	6988	36.42
37	11.46	10 55.3	36.73	1.58	0.66	1.11	36.61	6693	36.72
37	11.58	11 26.5	36.02	1.66	0.95	2.25	36.08	6143	36.14
37	11.59	10 42.4	36.72	1.05	0.51	0.89	36.69	7626	36.73
37	11.75	13 0.5	35.81	0.73	–0.97	0.16	35.72	15873	35.89
37	11.79	15 14.6	36.62	1.39	0.59	1.07	36.55	6000	36.52
37	11.81	10 19.5	36.14	1.94	0.10	1.07	36.06	7743	36.12
37	12.38	12 13.1	35.02	0.20	0.84	–0.26	34.96	5849	35.14
37	12.63	13 57.3	36.46	1.22	0.03	0.68	36.33	9187	36.49
37	12.68	12 23.0	36.22	1.85	0.74	1.20	36.06	6120	36.20
37	12.68	15 42.8	36.63	2.48	0.73	1.74	36.43	5669	36.56
37	12.68	15 46.1	37.07	1.84	1.07	1.44	36.92	5499	37.03
37	12.96	10 28.6	36.73	2.11	1.12	1.81	36.60	5642	36.67
37	13.00	12 9.5	36.02	1.44	0.45	0.27	35.76	5973	35.97
37	13.10	13 33.9	36.83	1.42	0.51	0.95	36.71	7182	36.83

Table 1—Continued

RA (−12h)	Dec ^a (−62°)	log[L(B)] (W) ^b	α_{UV} (2p)	α_{IR} (2p)	α_{UV} (sBB)	log(L(λ_m :blue) (W)	T (sBB)	log(L(λ_m :red) (W)
37 13.30	10 54.3	36.99	0.79	0.60	0.54	36.94	7052	37.03
37 13.21	14 4.7	35.75	2.18	1.01	2.12	35.69	5551	35.80
37 13.31	13 56.4	36.83	0.27	0.38	0.27	36.87	8385	36.87
37 13.70	15 11.3	36.64	3.11	1.29	2.67	36.47	4924	36.56
37 13.79	14 24.5	36.23	3.27	1.86	3.66	36.18	4663	36.30
37 13.85	13 35.2	36.94	1.75	0.72	1.37	36.81	6322	36.91
37 14.12	10 44.4	36.70	0.92	0.17	0.58	36.63	9086	36.79
37 14.25	10 50.0	36.24	1.36	0.25	2.20	36.37	8840	36.29
37 14.38	12 21.2	36.66	2.67	1.43	2.92	36.61	5440	36.61
37 14.48	15 29.8	37.10	6.87	1.04	6.63	36.77	4952	36.86
37 15.07	13 34.1	36.51	0.86	0.73	0.68	36.47	7317	36.59
37 15.49	12 12.2	37.06	4.92	1.31	5.32	36.92	4954	36.92
37 15.71	14 16.7	36.74	1.65	0.72	1.26	36.64	6310	36.72
37 15.92	11 59.1	36.34	4.75	1.18	5.24	36.25	4564	36.19
37 15.91	12 13.3	36.86	3.23	2.18	3.23	36.75	4176	36.75
37 16.02	13 43.5	36.49	1.88	1.13	1.43	36.35	5658	36.51
37 16.37	13 53.1	36.28	1.47	0.62	1.36	36.29	6736	36.39
37 16.21	13 47.3	36.40	1.34	0.92	1.20	36.40	6107	36.50
37 16.34	14 32.8	36.30	0.97	−0.72	0.55	36.24	13241	36.37
37 16.63	15 11.4	37.03	3.01	1.09	3.27	36.80	5804	36.98
37 16.72	13 10.3	36.75	1.56	0.81	1.08	36.60	7026	36.76
37 16.39	15 12.2	35.87	3.15	2.34	2.95	35.74	3781	35.79
37 16.70	10 42.2	36.90	0.93	0.37	0.70	36.84	8659	36.97
37 17.27	13 56.5	36.30	1.82	0.51	1.63	36.23	6795	36.29
37 17.15	11 22.6	36.43	5.84	1.40	5.99	36.22	4881	36.31
37 17.14	13 52.2	37.00	1.86	1.05	1.69	36.94	6110	36.94
37 17.22	15 12.1	35.48	1.88	−0.39	2.04	35.46	9482	35.47
37 17.38	10 46.8	35.32	0.78	0.66	0.95	35.34	5763	35.19
37 17.65	11 14.2	37.45	6.00	1.29	5.27	37.06	4768	37.27
37 17.74	11 27.3	35.25	2.15	0.43	2.55	35.24	7693	35.21
37 17.77	14 39.4	36.32	2.48	1.25	2.48	36.25	5379	36.32
37 18.05	12 48.3	36.78	2.76	1.68	2.17	36.52	4719	36.69
37 18.29	11 50.7	35.28	3.76	0.58	4.76	35.25	5527	35.15
37 18.43	13 28.7	35.79	2.61	1.57	2.61	35.71	4973	35.82

Table 1—Continued

RA (−12h)	Dec ^a (−62°)	log[L(B)] (W) ^b	α_{UV} (2p)	α_{IR} (2p)	α_{UV} (sBB)	log(L(λ_m :blue)) (W)	T (sBB)	log(L(λ_m :red)) (W)
37 18.58	13 47.8	36.00	1.47	0.72	0.96	35.89	6213	35.97
37 18.65	13 21.7	36.55	4.58	1.55	4.53	36.37	4608	36.47
37 19.13	11 31.1	37.14	2.95	1.24	2.52	36.98	4877	37.04
37 19.12	13 8.8	35.59	1.32	0.71	1.48	35.62	6580	35.65
37 19.04	13 15.4	36.46	0.10	−0.21	0.31	36.56	51363	36.51
37 19.28	11 43.5	36.47	1.14	0.59	0.79	36.38	6496	36.49
37 19.23	12 36.3	36.05	2.29	0.99	2.00	35.95	5579	36.01
37 19.60	12 4.8	35.19	3.00	0.22	2.47	35.07	6494	35.09
37 19.60	12 56.2	36.67	3.27	1.04	2.85	36.46	5768	36.59
37 19.64	13 37.6	36.62	3.25	2.00	3.52	36.58	4307	36.63
37 20.87	13 40.5	36.77	1.31	0.23	1.26	36.74	8489	36.74
37 21.15	13 43.7	36.99	0.55	0.16	0.55	37.02	10116	37.02
37 21.23	12 47.3	36.76	2.88	0.57	1.92	36.63	5454	36.58
37 21.40	11 20.3	36.47	1.23	0.41	0.20	36.23	7163	36.46
37 21.53	13 34.8	36.95	5.64	1.83	7.43	37.13	5125	37.14
37 21.78	12 25.4	36.35	2.05	1.17	1.82	36.26	5531	36.37
37 22.38	11 45.5	36.33	1.00	0.82	0.36	36.20	6318	36.36
37 22.48	12 16.0	37.09	2.70	1.79	2.76	37.01	4676	37.01
37 22.61	13 56.7	37.16	1.49	1.39	1.42	37.12	5446	37.12
37 22.59	11 56.7	36.26	1.42	1.23	1.40	36.24	5540	36.34
37 23.05	13 39.0	36.56	0.79	0.67	1.11	36.66	8122	36.66
37 23.46	13 33.0	36.49	4.01	0.84	2.85	36.16	5354	36.35
37 3.29	16 46.6	36.67	1.61	0.34	1.40	36.59	7243	36.64
37 4.61	16 51.8	36.77	3.13	0.96	1.51	36.53	5189	36.63
37 8.15	16 59.5	36.82	4.14	1.30	3.09	36.49	4517	36.65
37 11.99	16 59.6	37.06	1.81	1.00	1.81	37.02	5882	37.02
37 14.38	15 59.3	36.76	2.16	1.18	0.67	36.47	5142	36.68
37 16.67	16 44.4	36.43	1.68	1.46	0.75	36.21	4674	36.34
37 16.82	10 7.4	36.77	2.02	0.68	0.62	36.69	6588	36.70
37 18.45	15 53.7	36.83	3.25	0.62	1.74	36.46	5558	36.66
37 18.78	16 4.8	36.52	2.51	0.60	1.58	36.28	5988	36.46
37 22.24	11 24.1	36.71	1.78	0.54	1.45	36.59	6494	36.66
36 38.43	12 31.2	36.87	4.10	1.26	4.49	36.79	5358	36.71
36 38.61	12 33.8	36.18	1.99	0.55	2.32	36.21	7845	36.14

Table 1—Continued

RA (−12h)	Dec ^a (−62°)	log[L(B)] (W) ^b	α_{UV} (2p)	α_{IR} (2p)	α_{UV} (sBB)	log(L(λ_m :blue)) (W)	T (sBB)	log(L(λ_m :red)) (W)
36 38.99	12 19.7	36.43	1.75	0.81	0.65	36.15	6329	36.37
36 40.02	12 7.3	37.17	4.09	1.19	3.73	36.97	5617	37.04
36 40.85	12 3.1	36.50	0.75	0.76	0.58	36.48	7647	36.54
36 40.94	12 5.3	36.63	1.47	−0.13	1.27	36.57	8350	36.46
36 41.34	11 40.8	36.32	2.87	1.73	2.35	36.13	4505	36.10
36 41.43	11 42.5	35.92	2.32	2.25	1.18	35.63	3700	35.59
36 41.62	12 0.5	35.16	3.08	0.24	2.07	34.96	7150	35.01
36 41.62	11 31.7	35.77	2.54	0.28	2.10	35.78	6954	35.69
36 41.95	12 5.4	36.63	2.48	0.99	1.98	36.49	5469	36.49
36 42.93	12 16.4	36.79	2.33	0.80	1.73	36.67	6074	36.70
36 43.16	12 42.2	37.11	5.25	1.58	4.72	36.79	4791	36.92
36 43.21	11 48.1	37.01	3.52	2.00	3.18	36.83	4595	36.88
36 43.42	11 51.4	36.82	0.38	0.98	0.33	36.83	7424	36.89
36 43.61	12 18.1	36.46	1.31	0.67	1.12	36.38	7065	36.43
36 43.81	11 42.9	37.32	6.09	1.47	5.99	37.06	4896	37.13
36 43.97	12 50.1	36.89	2.86	1.22	1.98	36.63	5237	36.74
36 44.19	12 40.3	36.36	0.82	0.21	0.28	36.22	8967	36.36
36 44.20	12 47.8	36.65	1.25	0.38	0.69	36.55	7553	36.59
36 44.38	11 33.2	37.76	6.16	1.67	6.22	37.45	4611	37.52
36 44.49	11 42.3	36.68	1.72	0.89	1.27	36.66	7225	36.71
36 44.83	12 0.1	35.89	2.20	0.48	1.25	35.66	6635	35.76
36 45.01	12 39.6	36.39	0.82	1.15	0.63	36.36	6456	36.40
36 45.96	12 1.3	35.85	1.52	0.91	1.01	35.76	6885	35.89
36 46.13	12 46.5	36.92	4.10	1.19	3.51	36.62	5481	36.76
36 46.17	11 42.2	37.39	1.86	2.03	1.50	37.29	4876	37.33
36 46.34	14 4.6	37.25	2.73	1.91	2.54	37.16	5238	37.28
36 46.51	12 3.5	35.44	1.23	−0.23	0.91	35.36	9890	35.37
36 46.51	11 51.3	36.42	5.59	1.07	4.93	36.07	5017	36.16
36 46.50	14 7.5	34.45	1.65	0.04	0.83	34.34	8462	34.34
36 46.80	11 44.9	36.55	1.15	0.88	0.77	36.53	7270	36.58
36 47.00	12 36.9	36.40	2.33	0.52	1.67	36.21	6051	36.19
36 47.10	12 12.5	35.51	0.59	0.48	0.16	35.46	7839	35.44
36 47.16	14 14.4	35.82	2.63	1.80	2.48	35.67	4657	35.71
36 47.28	12 30.7	35.91	1.85	0.47	0.77	35.70	6573	35.77

Table 1—Continued

RA (−12h)	Dec ^a (−62°)	log[L(B)] (W) ^b	α_{UV} (2p)	α_{IR} (2p)	α_{UV} (sBB)	log(L(λ_m :blue) (W)	T (sBB)	log(L(λ_m :red) (W)
36 47.55	12 52.7	35.73	0.99	0.48	0.98	35.71	9128	35.85
36 47.79	12 32.9	36.48	1.66	1.03	0.84	36.24	6313	36.43
36 48.07	13 9.0	36.92	6.87	1.24	5.55	36.66	5057	36.74
36 48.29	14 26.3	36.41	1.62	0.42	1.54	36.36	6406	36.27
36 48.33	12 14.3	36.75	1.52	1.07	0.44	36.52	6351	36.73
36 48.62	13 28.1	36.68	1.66	0.64	0.91	36.45	7382	36.67
36 48.77	13 18.4	36.40	1.24	0.57	0.93	36.30	7311	36.38
36 48.98	12 45.8	35.76	1.86	0.21	0.59	35.49	7617	35.65
36 49.05	12 21.1	36.81	1.08	0.71	0.50	36.67	7162	36.80
36 49.24	11 48.8	36.69	2.13	1.75	1.30	36.43	4966	36.59
36 49.34	11 55.1	36.40	0.09	0.52	−0.31	36.33	8153	36.44
36 49.36	13 11.2	36.85	1.69	1.71	1.33	36.13	6208	36.17
36 49.43	13 16.5	36.85	1.69	1.71	1.39	36.75	5118	36.77
36 49.43	13 46.8	36.32	5.96	0.78	4.78	35.96	4985	36.00
36 49.57	12 20.0	36.07	0.86	0.54	1.02	36.09	7218	36.04
36 49.49	14 6.6	36.83	2.18	1.45	1.89	36.70	5191	36.72
36 49.63	12 57.6	36.31	2.65	1.29	1.70	36.03	4884	36.10
36 49.70	13 13.0	36.48	3.28	1.47	2.80	36.23	4709	36.28
36 49.86	12 42.3	35.64	0.21	−0.30	0.53	35.76	13592	35.77
36 49.95	12 25.9	36.44	0.42	0.81	0.18	36.38	7089	36.41
36 50.15	12 16.9	36.86	3.76	1.71	3.07	36.54	4780	36.70
36 50.19	12 39.8	36.88	2.39	0.62	1.13	36.69	6391	36.78
36 50.20	13 41.7	36.18	0.53	0.94	0.38	36.13	6817	36.09
36 50.26	12 45.7	36.86	4.90	1.57	4.83	36.55	4857	36.71
36 50.34	14 18.5	36.38	1.39	0.52	0.75	36.21	7339	36.29
36 50.48	13 16.1	36.64	2.99	1.68	2.47	36.41	4818	36.50
36 50.83	12 51.5	35.87	2.81	0.37	1.19	35.66	6991	35.75
36 50.82	12 55.8	35.83	1.49	0.13	0.72	35.69	7576	35.71
36 51.04	13 20.6	36.53	2.25	0.39	1.86	36.43	6569	36.40
36 51.40	13 0.6	34.38	1.71	0.39	3.14	34.44	6960	34.34
36 51.37	14 20.9	35.74	1.54	0.33	0.40	35.50	6991	35.60
36 51.69	12 20.2	36.32	3.38	1.12	3.21	36.15	5100	36.12
36 51.77	13 53.7	36.80	2.89	1.42	2.43	36.61	5039	36.66
36 51.99	12 9.6	35.94	1.84	0.35	0.51	35.66	6909	35.80

Table 1—Continued

RA (−12h)	Dec ^a (−62°)	$\log[L(B)]$ (W) ^b	α_{UV} (2p)	α_{IR} (2p)	α_{UV} (sBB)	$\log(L(\lambda_m:\text{blue}))$ (W)	T (sBB)	$\log(L(\lambda_m:\text{red}))$ (W)
36 51.96	13 32.1	36.76	1.88	1.16	1.72	36.67	6076	36.68
36 51.96	14 0.7	36.00	2.29	0.96	1.61	35.80	5857	35.91
36 52.66	12 19.7	35.72	1.92	0.45	0.73	35.48	6385	35.54
36 52.72	13 54.7	37.33	0.33	0.65	0.26	37.34	8663	37.39
36 52.84	14 4.8	35.82	2.21	1.00	0.83	35.49	5361	35.61
36 53.43	12 34.3	36.11	2.14	0.91	1.48	35.90	5977	36.01
36 53.65	14 17.6	35.82	2.19	0.49	1.55	35.62	6878	35.75
36 53.88	12 54.0	37.01	2.67	1.49	2.02	36.78	5117	36.91
36 54.07	13 54.2	36.70	1.77	1.00	1.24	36.54	6041	36.64
36 54.96	13 14.8	35.68	1.51	0.30	1.83	35.70	7333	35.60
36 55.14	13 3.7	36.51	3.82	1.70	3.58	36.15	4739	36.34
36 55.30	13 11.3	35.33	1.48	0.50	3.33	35.27	3435	35.26
36 55.39	13 11.0	36.91	3.73	2.55	3.51	36.77	4499	36.92
36 55.49	14 2.6	35.96	2.88	1.39	2.65	35.76	5286	35.89
36 55.59	12 46.2	36.79	2.54	1.20	1.37	36.60	5549	36.72
36 55.51	13 53.3	36.90	0.85	1.07	0.71	36.87	6481	36.89
36 55.59	12 49.3	36.48	0.99	0.54	0.19	36.26	7689	36.50
36 55.55	13 59.8	35.73	1.18	0.52	1.01	35.65	6945	35.70
36 56.10	13 29.6	36.70	1.02	1.12	0.95	36.67	6688	36.74
36 56.61	12 20.1	36.87	3.92	1.75	3.19	36.54	4738	36.71
36 56.62	12 45.5	37.16	6.10	1.47	4.74	36.89	4754	36.97
36 56.61	12 52.7	36.68	1.12	2.14	0.60	36.53	5100	36.69
36 56.90	12 58.0	35.76	3.43	0.73	3.06	35.58	5979	35.59
36 56.89	13 1.5	35.80	1.83	2.21	0.49	35.49	3749	35.46
36 57.18	12 25.9	36.27	1.33	0.57	0.30	36.03	6788	36.20
36 57.27	12 59.5	36.61	1.38	0.39	0.73	36.48	7266	36.54
36 57.69	13 15.3	36.62	0.99	0.83	0.74	36.54	7312	36.59
36 58.04	13 0.4	35.89	1.13	0.21	0.89	35.80	7392	35.78
36 58.63	12 21.8	36.03	0.91	0.77	0.68	35.96	7121	36.06
36 58.73	12 52.4	36.27	2.18	0.54	2.02	36.04	5845	36.03
36 59.41	12 21.5	35.67	1.30	−0.26	0.08	35.43	9999	35.62
37 0.53	12 34.7	36.74	5.31	1.14	4.75	36.41	5096	36.52

^aJ2000 coordinates

^b $M_B = -21.0$ (rest frame) $\equiv \log[L(B) \text{ (W)}] = 36.9$.

Table 2. Median Spectral Indices for Objects in the Region of the HDF Using the 2p SED Model

Number	\mathcal{A}	\mathcal{I} α_{UV}	\mathcal{E}		\mathcal{A}	\mathcal{I} α_{IR}	\mathcal{E}
0.25 < z < 0.5							
155	4.5 (0.6) ^a	2.6 (0.1)	1.8 (0.1)		1.0 (0.1)	1.0 (0.1)	0.6 (0.1)
0.5 < z < 0.8							
199	5.3 (0.2)	2.6 (0.1)	1.4 (0.1)		1.4 (0.1)	1.2 (0.1)	0.6 (0.1)
0.8 < z < 1.05							
135	5.1 (0.7)	2.8 (0.3)	1.3 (0.1)		1.3 (0.1)	1.3 (0.1)	0.8 (0.1)
1.05 < z < 1.5							
26	5.3 (1.0)	...	1.1 (0.2)		1.3 (0.2)	...	1.1 (0.1)

^aAll entries have the median followed in parentheses by the 1σ uncertainty of the median calculated assuming Gaussian statistics holds.

Table 3. Median Spectral Indices for Objects in the Region of the HDF Using the sBB SED Model

Number	\mathcal{A}	\mathcal{I} α_{UV}	\mathcal{E}		\mathcal{A}	\mathcal{I} T	\mathcal{E}
0.25 < z < 0.5							
155	4.4 (0.7) ^a	2.2 (0.1)	1.4 (0.1)		5125 (100)	5400 (100)	6575 (100)
0.5 < z < 0.8							
199	4.8 (0.3)	1.9 (0.1)	1.0 (0.1)		4875 (100)	5300 (100)	6600 (100)
0.8 < z < 1.05							
135	4.7 (0.6)	2.8 (0.3)	1.0 (0.1)		4900 (100)	4950 (100)	6700 (100)
1.05 < z < 1.5							
26	4.3 (1.0)	...	0.7 (0.2)		4600 (300)	...	6100 (200)

^aAll entries have the median followed in parentheses by the 1σ uncertainty of the median calculated assuming Gaussian statistics holds.

Table 4. Median R Luminosity as a Function of Spectral Index for Objects in the Region of the HDF (2p SED Model)

Range of α_{UV}	Number	Median Log[L(R)] (Watts)	Range of α_{IR}	Number	Median Log[L(R)] (Watts)
$0.25 \leq z < 0.5$					
0 – 1	9	35.50 (0.1)	–2 – –1	0	...
1 – 2	50	35.83 (0.1)	–1 – 0	14	35.47 (0.1)
2 – 3	48	36.11 (0.1)	0 – 1	83	35.98 (0.1)
3 – 4	27	36.25 (0.1)	1 – 2	53	36.38 (0.1)
4 – 5	12	36.64 (0.1)	2 – 3	5	35.77 (0.2)
5 – 6	5	36.60 (0.1)	4 – 5	0	...
$0.5 \leq z < 0.8$					
0 – 1	17	35.85 (0.1)	–2 – –1	0	...
1 – 2	75	36.32 (0.1)	–1 – 0	6	35.63 (0.1)
2 – 3	59	36.47 (0.1)	0 – 1	109	36.29 (0.1)
3 – 4	16	36.75 (0.1)	1 – 2	84	36.79 (0.1)
4 – 5	10	36.81 (0.1)	2 – 3	0	...
5 – 6	13	36.69 (0.1)	4 – 5	0	...
$0.8 \leq z < 1.05$					
0 – 1	34	36.46 (0.1)	–2 – –1	0	...
1 – 2	55	36.65 (0.1)	–1 – 0	4	36.27 (0.1)
2 – 3	21	36.91 (0.1)	0 – 1	65	36.57 (0.1)
3 – 4	11	37.02 (0.1)	1 – 2	63	36.99 (0.1)
4 – 5	3	37.06 (0.2)	2 – 3	4	36.90 (0.1)
5 – 6	7	37.15 (0.1)	4 – 5	0	...
$1.05 \leq z < 1.5$					
0 – 1	11	36.47 (0.1)	–2 – –1	1	37.03 (...)
1 – 2	10	36.86 (0.1)	–1 – 0	2	36.65 (0.1)
2 – 3	3	36.66 (0.2)	0 – 1	5	36.34 (0.2)
3 – 4	0	...	1 – 2	15	36.91 (0.1)
4 – 5	1	37.41 (...)	2 – 3	3	36.68 (0.2)
5 – 6	0	...	4 – 5	0	...

^aAll entries have the median followed by the 1σ uncertainty in the median computed assuming Gaussian statistics applies.

Table 5. Median Blue Luminosity as a Function of Spectral Index for Objects in the Region of the HDF (sBB Model)

Range of α_{UV}	Number	Log[L(λ_m : red)] (Median, Watts)	Range of $T(sBB)$	Number	Log[L(λ_m : red)] (Median, Watts)
$0.25 \leq z < 0.5$					
–1 – 0	1	35.14 (...)	3800 – 4375	8	35.89 (0.2)
0 – 1	29	35.76 (0.1)	4375 – 5025	26	36.47 (0.1)
1 – 2	59	36.04 (0.1)	5025 – 5775	42	36.24 (0.1)
2 – 3	36	36.14 (0.1)	5775 – 6650	33	36.03 (0.1)
3 – 4	17	36.30 (0.1)	6650 – 7650	28	35.78 (0.1)
4 – 5	5	36.39 (0.1)	7650 – 8800	7	35.62 (0.1)
5 – 6	6	36.51 (0.2)	8800 – 10125	4	35.47 (0.1)
$0.5 \leq z < 0.8$					
–1 – 0	5	35.76 (0.1)	3800 – 4375	5	36.65 (0.1)
0 – 1	52	36.21 (0.1)	4375 – 5025	39	36.74 (0.1)
1 – 2	67	36.46 (0.1)	5025 – 5775	52	36.51 (0.1)
2 – 3	36	36.56 (0.1)	5775 – 6650	50	36.29 (0.1)
3 – 4	11	36.52 (0.2)	6650 – 7650	35	36.38 (0.1)
4 – 5	14	36.54 (0.1)	7650 – 8800	10	36.15 (0.1)
5 – 6	9	36.67 (0.1)	8800 – 10125	5	36.19 (0.2)
6 – 10	4	36.74 (0.1)			
$0.8 \leq z < 1.05$					
–1 – 0	3	35.87 (0.1)	3800 – 4375	3	36.61 (0.1)
0 – 1	49	36.56 (0.1)	4375 – 5025	31	36.92 (0.1)
1 – 2	45	36.72 (0.1)	5025 – 5775	22	36.87 (0.1)
2 – 3	17	36.73 (0.1)	5775 – 6650	20	36.30 (0.1)
3 – 4	9	36.75 (0.1)	6650 – 7650	33	36.63 (0.1)
4 – 5	5	36.92 (0.1)	7650 – 8800	16	36.59 (0.1)
5 – 6	5	36.92 (0.1)	8800 – 10125	6	36.49 (0.2)
6 – 10	5	37.01 (0.1)	>10125	6	36.51 (0.2)
$1.05 \leq z < 1.5$					
–1 – 0	1	36.51 (...)	3800 – 4375	0	
0 – 1	13	36.69 (0.1)	4375 – 5025	5	36.96 (0.2)
1 – 2	8	36.96 (0.1)	5025 – 5775	4	36.64 (0.1)
2 – 3	3	36.57 (0.1)	5775 – 6650	7	36.77 (0.2)
3 – 4	0	...	6650 – 7650	7	36.58 (0.2)
4 – 5	0	...	7650 – 8800	1	37.39 (...)
5 – 6	0	...	8800 – 10125	0	

Table 5—Continued

Range of α_{UV}	Number	Log[L(λ_m : red)] (Median, Watts)	Range of $T(sBB)$	Number	Log[L(λ_m : red)] (Median, Watts)
6 – 10	1	37.52 (...)	>10125	3	36.51 (0.1)

^aAll entries have the median followed by the 1σ uncertainty in the median computed assuming Gaussian statistics applies.

Table 6a. Additional Redshifts for Galaxies in the Flanking Fields of the HDF

RA (–12h)	Dec ^a (–62°)	R (mag)	z	Quality	Sp.Type	Source
36 16.67	13 10.5	23.34	0.437	1	\mathcal{E}	cal
36 18.16	12 57.6	23.54	0.473	1	\mathcal{E}	cal
36 21.69	12 18.2	23.32	1.008	1	\mathcal{E}	cal
36 22.86	11 18.4	23.78	0.895	5	\mathcal{E}	cal
36 22.85	14 51.3	23.50	0.652	1	\mathcal{E}	cal
36 23.98	11 21.6	23.53	0.842	4	\mathcal{E}	cal
36 25.14	12 27.5	23.63	1.091	3	\mathcal{A}	cal
36 25.97	12 37.6	23.63	0.437	1	\mathcal{EI}	cal
36 27.50	10 26.0	23.43	0.763	3	\mathcal{I}	cal
36 29.75	12 0.3	23.16	1.016	1	\mathcal{EI}	cal
36 29.82	11 53.4	23.17	0.529	1	\mathcal{E}	cal
36 33.23	10 49.9	23.34	1.006	1	\mathcal{E}	cal
36 36.69	11 11.3	23.24	0.846	1	\mathcal{E}	cal
36 37.07	16 15.1	23.56	0.852	1	\mathcal{E}	cal
36 37.72	9 45.8	23.39	0.513	1	\mathcal{E}	cal
36 38.60	12 53.3	23.41	0.960	5	\mathcal{E}	cal
36 39.47	10 16.0	23.33	0.485	1	\mathcal{E}	cal
36 41.42	10 51.2	23.38	0.937	1	\mathcal{E}	cal
36 42.34	16 22.3	23.34	0.855	1	\mathcal{E}	cal
36 42.84	14 12.1	23.43	0.586	1	\mathcal{E}	cal
36 43.24	13 32.5	23.43	0.905	4	\mathcal{E}	cal
36 44.42	10 52.8	23.50	0.937	1	\mathcal{E}	cal
36 45.24	11 8.7	23.41	0.513	1	\mathcal{EI}	cal
36 46.56	10 49.1	23.70	0.857	3	\mathcal{I}	cal
36 48.57	10 48.8	23.39	0.940	5	\mathcal{E}	cal
36 49.75	11 6.7	23.37	1.018	3	\mathcal{E}	cal
36 50.52	15 24.0	23.80	0.321	1	\mathcal{E}	cal
36 52.03	10 59.1	23.67	0.955	5	\mathcal{E}	cal
36 52.24	9 57.6	23.07	0.750	1	\mathcal{E}	cal
36 53.36	10 25.8	23.20	0.973	4	\mathcal{E}	cal
36 56.03	10 20.7	23.64	0.938	1	\mathcal{E}	cal
36 56.84	10 2.0	23.51	0.000	1	\mathcal{M}	cal
36 57.07	15 11.2	23.50	0.849	1	\mathcal{EI}	cal
36 57.30	10 26.1	23.29	0.847	5	\mathcal{E}	cal

Table 6a—Continued

RA (−12h)	Dec ^a (−62°)	<i>R</i> (mag)	<i>z</i>	Quality	Sp.Type	Source
36 57.70	10 40.9	23.24	1.416	3	\mathcal{A}	cal
36 58.52	15 53.3	23.55	0.457	1	\mathcal{E}	cal
36 59.83	9 47.9	23.04	0.679	1	\mathcal{E}	cal
37 00.16	16 15.1	22.83	0.914	1	\mathcal{E}	cal
37 00.42	10 1.6	23.26	0.791	5	\mathcal{E}	cal
37 00.77	11 33.7	23.27	0.305	1	\mathcal{E}	cal
37 00.90	10 28.4	22.27	0.563	1	\mathcal{EI}	cal
37 01.11	14 26.0	23.41	0.901	4	\mathcal{E}	cal
37 02.24	10 33.0	23.46	0.276	1	\mathcal{E}	cal
37 02.53	11 5.3	23.43	1.014	1	\mathcal{E}	cal
37 04.25	9 59.7	22.59	0.322	1	\mathcal{E}	cal
37 04.27	10 29.9	23.23	0.411	1	\mathcal{E}	cal
37 06.04	13 40.4	23.25	0.672	5	\mathcal{E}	cal
37 06.33	10 57.4	23.66	0.906	1	\mathcal{E}	cal
37 06.83	10 6.6	22.89	0.938	4	\mathcal{E}	cal
37 09.64	11 19.4	23.76	1.176	1	\mathcal{E}	cal
37 10.54	11 16.3	23.60	0.841	5	\mathcal{E}	cal
37 11.14	12 57.0	23.20	0.484	1	\mathcal{E}	cal
37 12.15	11 44.2	23.10	0.909	4	\mathcal{E}	cal

^aJ2000 coordinates

^b $M_B = -21.0$ (rest frame) $\equiv \log[L(B) \text{ (W)}] = 36.9$.

Table 6b. Additional Redshifts for Galaxies in the HDF

RA (−12h)	Dec ^a (−62°)	R (mag)	z	Quality	Sp.Type	Source
36 37.77	12 35.1	23.87	0.485	1	\mathcal{E}	cal
36 45.30	11 42.9	24.00	0.558	1	\mathcal{E}	st0,cal
36 47.17	13 41.7	23.93	1.313	1	\mathcal{EA}	daw ^c
36 43.84	12 41.5	25.21	4.540	11	\mathcal{E}	stern ^d
36 44.66	11 50.2	26.50	4.580	11	\mathcal{E}	stern ^d

^aJ2000 coordinates

^b $M_B = -21.0$ (rest frame) $\equiv \log[L(B) (W)] = 36.9$.

^cPrivate communication, to be published by Dawson, Stern, Bunker, Spinrad & Dey (2000).

^dPublished in Stern & Spinrad (1999).

Table 7a. SED Parameters for Additional Galaxies in the Flanking Fields of the HDF

RA (–12h)	Dec ^a (–62°)		$\log[L(B)]$ (W) ^b	α_{UV} (2p)	α_{IR} (2p)	α_{UV} (sBB)	$\log(L(\lambda_m:\text{blue}))$ (W)	T (sBB)	$\log(L(\lambda_m:\text{red}))$ (W)
36 16.67	13	10.5	35.68	2.27	–0.34	1.09	35.54	9162	35.60
36 18.16	12	57.6	35.67	1.82	0.93	0.50	35.46	5281	35.51
36 21.69	12	18.2	36.60	1.61	0.96	1.73	36.61	6873	36.61
36 22.86	11	18.4	36.24	1.76	1.17	1.71	36.22	6255	36.29
36 22.85	14	51.3	36.01	2.12	0.77	1.60	35.91	6143	35.97
36 23.98	11	21.6	36.18	0.73	0.92	0.57	36.15	6708	36.25
36 25.14	12	27.5	36.50	2.18	–0.13	2.41	36.59	13001	36.59
36 25.97	12	37.6	35.37	1.39	0.77	1.02	35.29	6372	35.43
36 27.50	10	26.0	36.19	4.16	1.53	4.16	36.18	5732	36.26
36 29.75	12	0.3	36.53	0.08	0.89	0.18	36.56	6927	36.56
36 29.82	11	53.4	35.74	0.79	0.66	0.38	35.67	6915	35.82
36 33.23	10	49.9	36.58	1.30	1.19	1.66	36.64	6421	36.64
36 36.69	11	11.3	36.31	0.92	0.61	0.87	36.32	8018	36.44
36 37.07	16	15.1	36.22	1.33	1.22	1.33	36.21	6107	36.31
36 37.72	9	45.8	35.85	2.40	–0.40	0.40	35.58	8350	35.73
36 38.60	12	53.3	36.34	1.42	–0.26	1.17	36.37	12158	36.37
36 39.47	10	16.0	35.75	2.30	–0.02	0.66	35.53	6753	35.64
36 41.42	10	51.2	36.47	2.32	1.60	2.32	36.45	5699	36.64
36 42.34	16	22.3	36.43	3.38	0.82	3.38	36.45	7613	36.52
36 43.24	13	32.5	36.29	0.66	1.29	0.58	36.27	6278	36.40
36 44.42	10	52.8	36.31	0.86	0.60	0.84	36.32	8136	36.40
36 45.24	11	8.7	35.56	0.03	–0.22	–0.17	35.61	10293	35.76
36 46.56	10	49.1	36.32	2.83	2.59	2.78	36.24	4439	36.43
36 49.75	11	6.7	36.56	0.56	1.10	0.49	36.55	5826	36.55
36 52.03	10	59.1	36.33	1.09	1.24	1.69	36.46	6679	36.46
36 52.24	9	57.6	36.31	2.46	1.47	2.48	36.31	5119	36.31
36 53.36	10	25.8	36.54	0.94	0.84	1.19	36.60	7075	36.60
36 56.03	10	20.7	36.30	1.13	1.27	1.13	36.28	6664	36.47
36 57.07	15	11.2	36.24	1.10	1.16	1.00	36.22	6184	36.35
36 57.30	10	26.1	36.34	1.84	1.92	1.84	36.30	5459	36.52
36 57.70	10	40.9	37.25	3.14	0.75	3.65	37.44	9231	37.44
36 58.52	15	53.3	35.67	3.75	–0.34	2.10	35.49	8619	35.57
37 00.16	16	15.1	36.61	1.06	1.10	1.04	36.60	6556	36.60
37 00.42	10	1.6	36.24	0.74	1.04	0.68	36.21	6253	36.28

Table 7a—Continued

RA (−12h)	Dec ^a (−62°)		log[L(B)] (W) ^b	α_{UV} (2p)	α_{IR} (2p)	α_{UV} (sBB)	log(L(λ_m :blue)) (W)	T (sBB)	log(L(λ_m :red)) (W)
37 00.90	10	28.4	36.31	2.80	0.98	1.50	36.08	5429	36.22
37 01.11	14	26.0	36.32	0.80	0.98	0.70	36.31	6565	36.41
37 02.24	10	33.0	35.23	2.51	0.06	1.33	35.13	7636	35.15
37 02.53	11	5.3	36.37	0.13	−0.09	0.41	36.48	12724	36.48
37 04.25	9	59.7	35.69	2.84	−0.30	1.93	35.63	10928	35.68
37 04.27	10	29.9	35.67	2.05	−0.02	1.49	35.64	8218	35.62
37 06.04	13	40.4	36.21	2.19	−0.25	1.96	36.20	9040	36.15
37 06.33	10	57.4	36.27	0.96	0.66	0.93	36.29	8017	36.38
37 06.83	10	6.6	36.56	0.82	1.12	0.82	36.55	6209	36.67
37 09.64	11	19.4	36.66	1.23	1.41	1.22	36.64	5581	36.64
37 10.54	11	16.3	36.12	0.62	0.37	0.62	36.15	9395	36.30
37 11.14	12	57.0	35.61	0.37	1.15	0.37	35.60	6021	35.70
37 12.15	11	44.2	36.49	1.74	0.90	1.61	36.49	6268	36.50

^aJ2000 coordinates

^b $M_B = -21.0$ (rest frame) $\equiv \log[L(B) \text{ (W)}] = 36.9$.

Table 7b. SED Parameters for Additional Galaxies in the HDF

RA (−12h)	Dec ^a (−62°)		log[L(B)] (W) ^b	α_{UV} (2p)	α_{IR} (2p)	α_{UV} (sBB)	log(L(λ_m :blue)) (W)	T (sBB)	log(L(λ_m :red)) (W)
36 45.30	11	42.9	35.67	1.31	0.59	−0.03	35.43	6612	35.57
36 47.17	13	41.7	36.69	0.80	1.14	0.68	36.64	7056	36.73

^aJ2000 coordinates

^b $M_B = -21.0$ (rest frame) $\equiv \log[L(B) \text{ (W)}] = 36.9$.

Table 8. Corrections to Redshifts for Galaxies in the HDF

	RA	Dec ^a		R	Adopted z	Quality	Sp.Type
	(–12h)	(–62°)		(mag)			
36	39.60	12	30.2	24.40	3.479	11	\mathcal{E}
36	49.43	13	16.5	23.63	1.238	3	\mathcal{E}
36	56.10	13	29.6	23.80	1.238	4	\mathcal{E}

^aJ2000 coordinates